Energy & Environmental Science

ROYAL SOCIETY OF CHEMISTRY

REVIEW

View Article Online
View Journal | View Issue

Cite this: *Energy Environ. Sci.*, 2023, **16**, 4812

Advances and challenges in single-site catalysts towards electrochemical CO_2 methanation

Jiexin Zhu, [ab] Lei Lv,[a] Shahid Zaman, [e] Xingbao Chen,[a] Yuhang Dai,[ab] Shenghua Chen, *[c] Guanjie He, [b] Dingsheng Wang *[d] and Liqiang Mai *[a]

Received 5th July 2023,
Accepted 13th September 2023

DOI: 10.1039/d3ee02196c

rsc.li/ees

Electrochemical CO_2 reduction to a valuable product is a sustainable and economical method towards carbon neutralization. Among the different products of the electrochemical CO_2 reduction reaction (CO_2RR), methane is an excellent energy carrier with a high combustion heat. However, for higher methane product selectivity it is crucial to avoid C–C coupling that leads to multi-carbon products. Thus, single-site catalysts (SSCs) with a single active site are ideal candidates. This review summarizes and discusses the current research progress and future application prospects of electrochemical CO_2 methanation on SSCs. The CO_2 methanation mechanism and primary activity descriptors are discussed in detail with an extensive overview of the coordination structure and design of SSCs, as well as their several *in situ* characterization methods for tracking the structural changes in SSCs. This review provides insights into the further exploitation of SSCs for selective CO_2 methanation that inspires the rational design of SSCs in electrochemical CO_2 methanation research.

Broder context

The electrochemical CO_2 reduction reaction powered by renewable energy offers a promising pathway to produce valuable chemical feedstocks which may control and utilize atmospheric CO_2 emissions. Among the CO_2RR products, CH_4 is a good energy carrier with the highest combustion heat of 56 kJ g^{-1}. To achieve high selectivity for CH_4, *CO–CO coupling on multiple sites should be avoided. Single site catalysts are ideal candidates for CO_2 methanation due to their site isolation properties. However, the deep reduction of CO_2 on a single site is difficult and the reaction mechanism is complex. Unrevealing the activity descriptors for CO_2 methanation can help us understand the reaction mechanism and propose appropriate design strategies for single site catalysts. In this review, we discuss the activity descriptors based on the reaction mechanism and the design strategies of single site catalysts. The development of *in situ* characterization methods is also discussed to monitor the structural changes of single site catalysts. This review provides a guideline for the design, characterization, and application of single site catalysts.

1. Introduction

The widespread consumption of fossil fuels poses an enormous risk to the global environment. Chemical industries manufacture chemical products using fossil fuel-derived feedstocks, accounting for 18% of today's industrial CO_2 emissions, with coal combustion being the primary source of CO_2.[1–4] A series of climatic changes have been triggered by the progressive increase in atmospheric CO_2 emissions, causing an increase in global temperatures. Meanwhile, it is indispensable to halt the average increase in global temperatures below 1.5 °C by reducing atmospheric CO_2 emissions.[5] Therefore, converting atmospheric CO_2 into valuable chemical feedstocks is a sustainable approach for controlling and utilizing atmospheric CO_2 emissions.[6] Moreover, electricity costs will drop significantly with the development of solar and wind energy conversion and storage. Therefore the electrochemical CO_2 reduction reaction (CO_2RR) driven by renewable energy presents a feasible route to manufacture valuable chemical feedstocks (Fig. 1).[7–17] A typical CO_2RR process comprises CO_2 conversion into a series of short carbon chain molecules such as carbon monoxide (CO), formic acid (HCOOH), methane (CH_4), ethylene (C_2H_4), ethanol (C_2H_5OH), propanol (C_3H_7OH), *etc.*[18–21]

[a] *State Key Laboratory of Advanced Technology for Materials Synthesis and Processing, Wuhan University of Technology, Wuhan 430070, China. E-mail: mlq518@whut.edu.cn*
[b] *Electrochemical Innovation Lab, Department of Chemical Engineering, University College London, London, WC1E 7JE, UK*
[c] *National Innovation Platform (Center) for Industry-Education Integration of Energy Storage Technology, School of Chemical Engineering and Technology, Xi'an Jiaotong University, Xi'an, 710049, P. R. China. E-mail: shenghchen@xjtu.edu.cn*
[d] *Department of Chemistry, Tsinghua University, Beijing 100084, China. E-mail: wangdingsheng@mail.tsinghua.edu.cn*
[e] *Department of Mechanical and Energy Engineering, Southern University of Science and Technology, Shenzhen 518055, China*

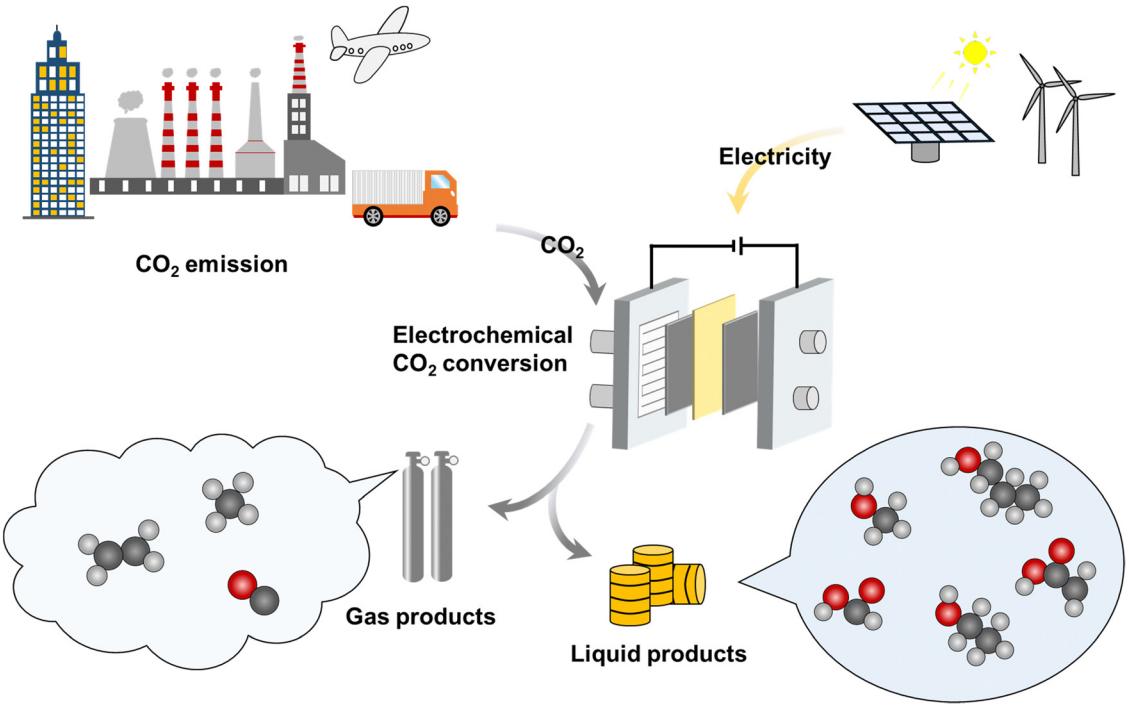

Fig. 1 CO_2 utilization pathway using electricity produced from renewable energy.

These molecule feedstocks can fuel or produce chemical products in traditional chemical enterprises.

Among the CO_2RR products, CH_4 is a suitable energy carrier with the highest combustion heat of 56 kJ g^{-1}.[22,23] It is also a main component of natural gas and a clean energy source that reduces the use of fossil fuels and can be used as feedstocks to produce carbon black, ammonia, urea, *etc.*[24] Besides, CH_4 is a typical greenhouse effect gas, and the greenhouse effect caused by 1% of methane will be greater than that of 99% of CO_2. Due to the unreasonable mining, a large amount of CH_4 is directly leaked into the atmosphere. Therefore, producing CH_4 from the CO_2RR can regulate the CO_2 level in the atmosphere and decrease natural gas utilization and leakage, thus reducing the greenhouse effect. Apart from electrochemical CO_2 methanation, thermocatalytic reduction of CO_2 to CH_4 with H_2 produced *via* water electrolysis is also a common way.[25–27] The electrochemical CO_2 reduction always proceeds at room temperature, whereas thermocatalytic CO_2 transformation typically necessitates high pressure and elevated temperatures, typically within the range of 200–300 °C. The high operating temperature costs a lot of energy, and H_2 produced by water electrolysis requires extra storage and transportation. In contrast, the electrochemical CO_2 methanation which consumes cheap electricity and protons from electrolytes represents a more economical and simpler route. For selective CH_4, the electrochemical CO_2RR involves eight-electron transfer with the standard equilibrium potential of 0.17 V *vs.* reversible hydrogen electrode (RHE), which is a more favorable product. However, due to the sluggish multi-electron transfer and electron–proton coupling efficiency, the practical activity for CO_2 methanation is far from the equilibrium potential.[28] Besides, the competitive relationship between the hydrogen evolution reaction (HER) further reduces the CO_2RR selectivity.

Therefore, it is vital to identify prospective electrocatalysts with high activity and selectivity to lower the energy barrier of CO_2 methanation.[29–31] Most electrocatalysts lack the ability to stabilize important intermediates such as *CHO and *COOC, which is required for the reduction reaction to progress beyond two-electron transfer, making copper (Cu)-based electrocatalysts superior.[20,32–45] However, Cu-based electrocatalysts are more vibrant to reduce CO_2 to ethanol and ethylene due to the facile *CO–CO coupling step on the Cu surface. Furthermore, the slow eight-electron transfer and the competitive HER both inhibit CO_2 methanation. As a result, it is challenging to attain high faradaic efficiency (FE) exceeding 90% on Cu electrocatalysts, which is much lower on other electrocatalysts.

Despite these problems, the FE for CO_2 methanation has significantly increased over the past decade, showing that 80% or higher FE is relatively simple to accomplish. It is found that a higher CO_2 methanation selectivity can be achieved on SSCs (Fig. 2).[35–39,46–57] We take for granted that isolated sites cannot achieve the *CO–CO coupling step so that the further reduction of *CO can proceed. The multi-electron transfer step can be pushed gradually through appropriate electronic structure optimizations. However, limited active sites, complex coordination structure, weak electron transfer capacity, and structural instability of SSCs restrict the CH_4 selectivity of the CO_2RR. To achieve higher FE for CH_4, it is vital to identify the critical CO_2 methanation parameters and the structure–activity relationship of SSCs.

This review systematically summarizes the recent advances and challenges of electrocatalytic CO_2 methanation on SSCs (Fig. 3). Firstly, we discuss the key parameters which greatly

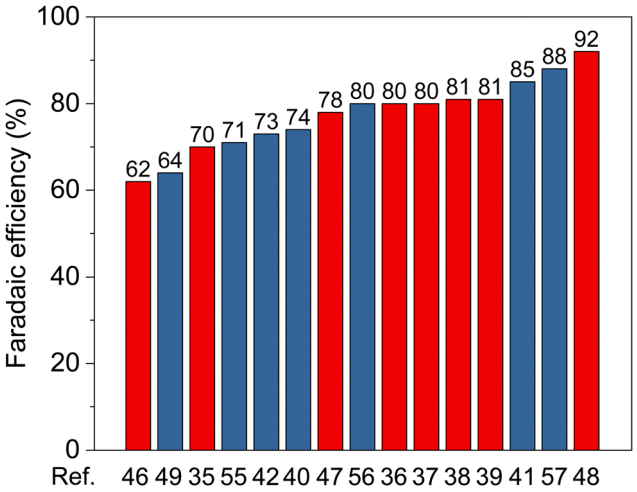

Fig. 2 The reported electrocatalysts with high CH_4 selectivity of the CO_2RR in recent years. The red columns represent the SSCs, and the blue columns represent the other catalysts.

influence the selectivity of CO_2 methanation, including catalyst factors: facet-dependence, size effect, and coordination number, and local reaction environment factors: local pH, anion/cation effect, and CO concentration. The recent advances of SSCs on different substrates for electrocatalytic CO_2 methanation, especially molecule-based and carbon-supported electrocatalysts, highlight the engineering of coordination and electronic structures. Furthermore, various *in situ* characterization methods for tracking the structural changes of SSCs during the CO_2RR are introduced, such as *in situ* XAS and *in situ* Raman spectroscopy. Finally, challenges and outlooks on electrocatalytic CO_2 methanation and industrialization are discussed.

2. Key parameters for electrocatalytic CO_2 methanation

The reduction of CO_2 to valuable products involves the transfer of multiple electrons and protons, and the product selectivity continuously decreases as the required number of electrons and protons increases. For the CH_4 product, eight electrons and protons are needed, indicating that CO_2 methanation is a high-energy barrier process. Although CO_2 methanation possesses the most positive thermodynamic potential than other products, it is also limited by the formation of a $*CO_2^-$ intermediate. The first electron transfer to the adsorbed $*CO_2$ shows an equilibrium potential as negative as −1.9 V (*vs.* standard hydrogen electrode, SHE). Therefore, the onset potential for CO_2 methanation is always more negative than that of CO, formic acid, and C_2H_4.[58,59] Thus, the reaction pathway of CO_2 methanation involves the *CO intermediate.[18,60,61] *CO is a key intermediate for many products that can be desorbed from the catalyst surface to form a CO molecule, or it can form a *CO–CO dimer and then be reduced to multi-carbon products like C_2H_4 and C_2H_5OH (Fig. 4). Thus, to obtain CH_4 in the subsequent step, the formation of *COH or *CHO is necessary.[62] The *COH pathway can only yield CH_4, while the *CHO pathway can also result in CH_3OH formation. Therefore, the direction of further

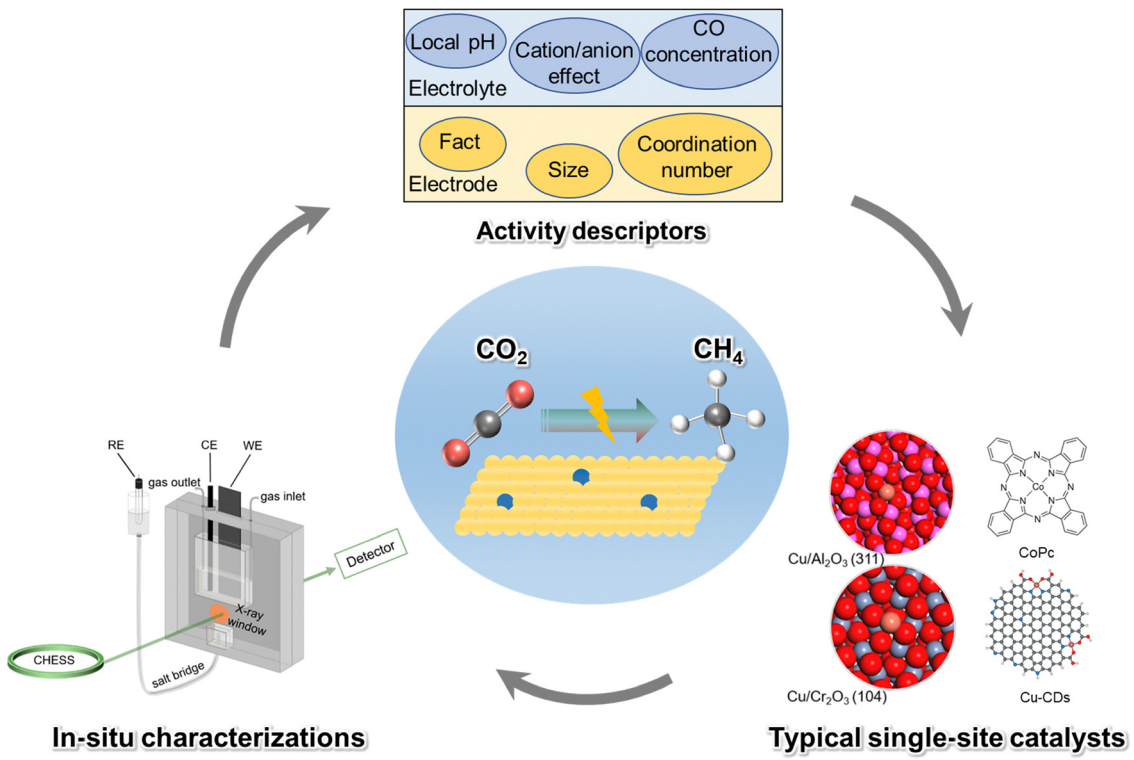

Fig. 3 A schematic outline of the key topics covered in this study.

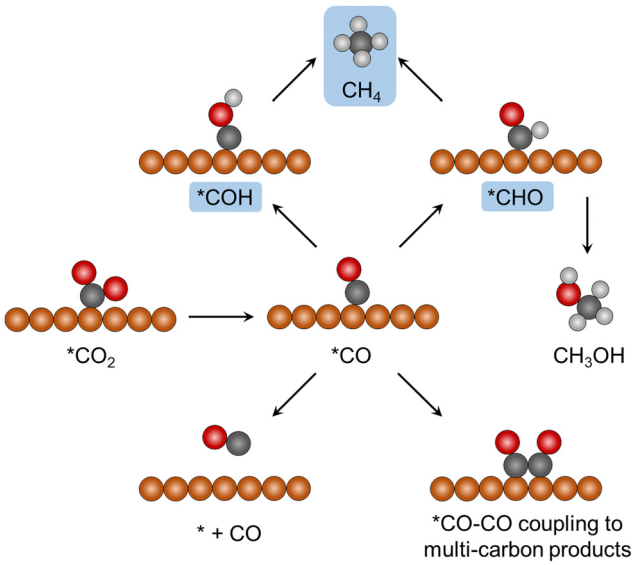

Fig. 4 The reaction pathways derived from the *CO intermediate on Cu-based catalysts.

reduction of the *CO intermediate is crucial for product selectivity. Several key parameters profoundly affect the reaction pathways for CO_2 methanation, including catalyst factors: facet-dependence, size effect, and coordination number, and local reaction environment factors: local pH, CO concentration, and anion/cation effect.

2.1 Facet-dependence

Facet-dependence is a common characteristic of many chemical reactions on metal catalysts.[63] Earlier experiments showed that CH_4 is formed more favorably on the Cu(100) surface, and C_2H_4 is predominantly produced on the Cu(111) surface.[64,65] Similarly, CH_4 formation is advantageous when the electrode is covered with abundant protons or hydrogen species.[58] Density functional theory (DFT) calculation has explored the specific impact of $H_3O^{\delta+}$ species on the product selectivity on Cu(100) and Cu(111) surfaces,[62] finding that the CO_2 is firstly adsorbed and reduced to *CO. However, the hydrogenation of *CO is different in each facet. On Cu(100), the formation of *CHO is favored and the product of ethylene is preferred by going through the C–C coupling of two *CHO intermediates. Cu(111) favors the formation of *COH, and methane is the dominant product. The formation of *CHO and *COH involves a H transferred from the solution to the adsorbed *CO intermediate. The supplied H comes from the metal surface for *CHO formation, while it comes from the water molecule in solution for *COH formation. The hydrogenation process shows different configurations on Cu(100) and Cu(111) (Fig. 5a and b). In transition states, two Cu atoms are close to the $H_3O^{\delta+}$ species on both Cu(100) and Cu(111). Due to the hexagonal configuration of the Cu(111) surface, additional two Cu atoms are close to $H_3O^{\delta+}$ species with distances of 2.62 and 2.81 Å (Fig. 5c). The different configurations result in the bonding of $H_3O^{\delta+}$ on Cu(100) an ionic bond and it is a covalent bond on Cu(111), which leads to a more stable $H_3O^{\delta+}$ on Cu(111) and reduces the barrier of *COH formation.

For SSCs, the facet-dependence is rarely discussed because the metal sites in SSCs are isolated. However, the coordination configuration of H towards *CO determined by facets can be extended to SCCs. Adjusting the ligand structure or coordinated atoms to the metal site can alter the bonding structure of the H species and *CO intermediate and steer the product selectivity.

2.2 Size effect

Tuning the size and shape of catalysts is a well-known strategy to alter the binding energy of the catalyst surface to reactants.[66–75] The size effect has been widely studied in thermocatalytic reactions, such as ammonia synthesis and hydrogenations.[76–78] However, it is challenging to determine the effect of nanoparticle size on the catalytic performance in electrocatalytic processes since the negative or positive potential always leads to structural reconstruction of electrocatalysts. The size effects on CH_4 selectivity for the CO_2RR were investigated by comparing the reconstruction and performances of Cu nanoparticles supported on glassy carbon (n-Cu/C) and Cu foil.[79] It is found that the n-Cu/C

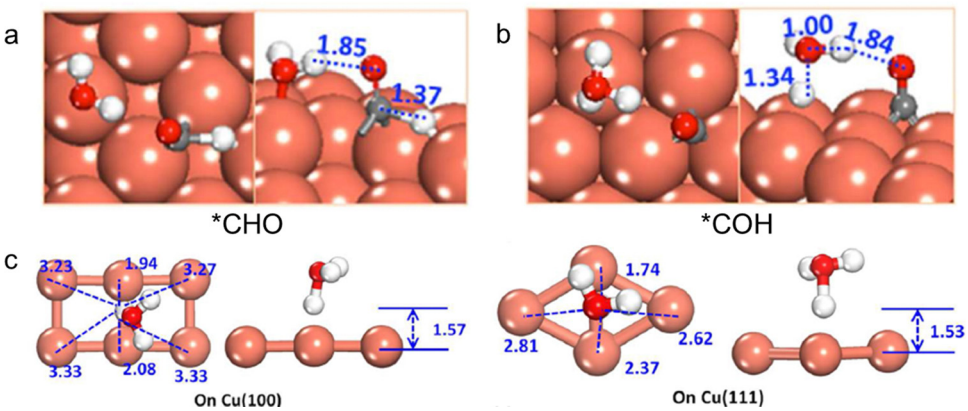

Fig. 5 Optimized structures of the transition states involved in *CO reduction to (a) *CHO with the water-solvated model on the Cu(100) facet and to (b) *COH with the H-shuttling model on the Cu(111) facet. (c) Closeup of the $H_3O^{\delta+}$ moiety in the transition state of COH* formation on Cu(100) and Cu(111). Reproduced with permission from Asthagiri *et al.*[62] Copyright 2016 American Chemical Society.

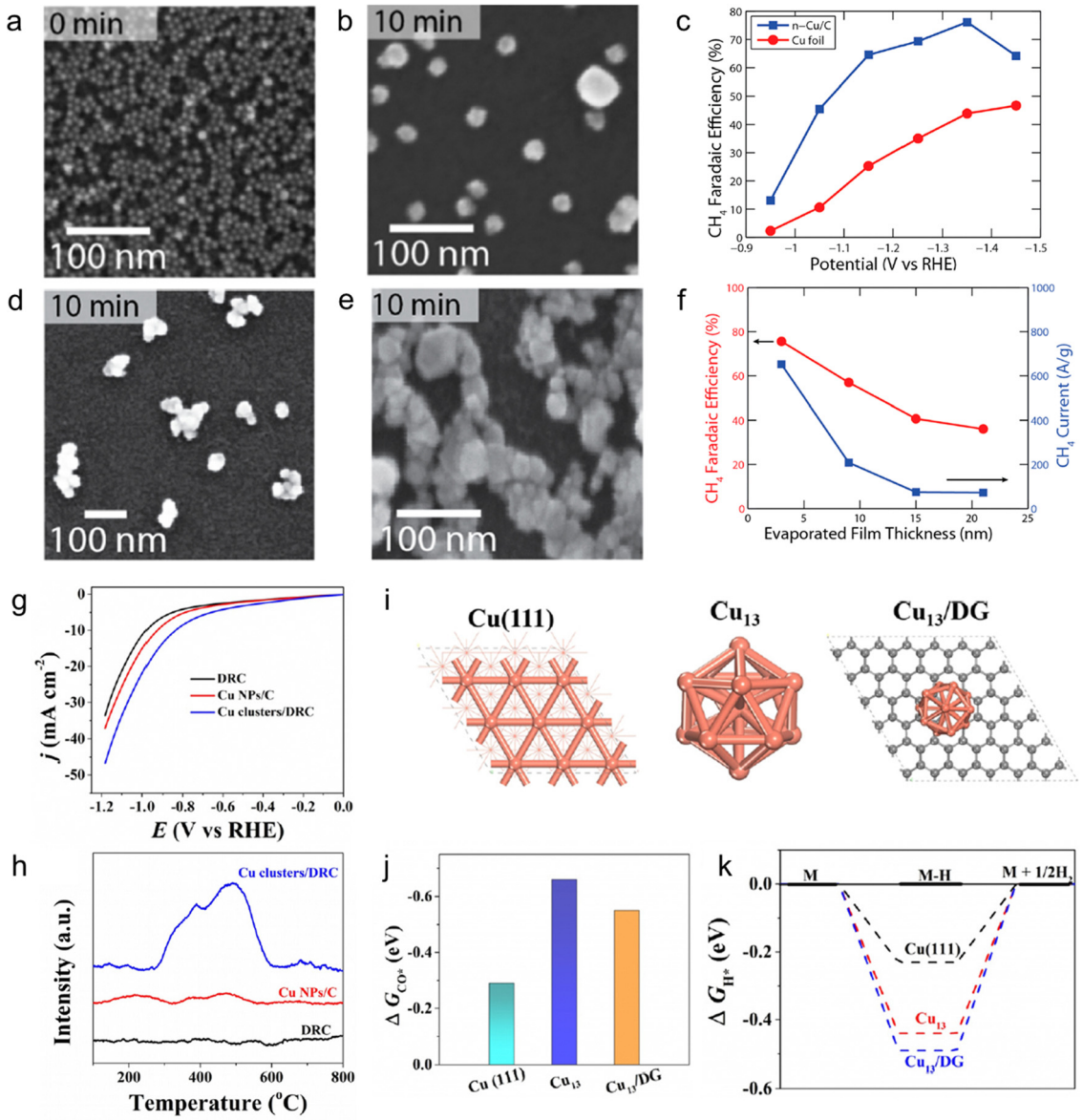

Fig. 6 (a) SEM image of the n-Cu/C electrode and (b) following operation for 10 min at −1.25 V *vs.* RHE under CO_2RR conditions. (c) FE for CH_4 on n-Cu/C Cu foil. (d) 3 nm evaporated Cu film after operating at −1.25 V for 10 min. (e) 15 nm evaporated Cu film after operating at −1.25 V for 10 min. (f) FE and mass current density for CH_4 as a function of the evaporated Cu film thickness. Reproduced with permission from Alivisatos *et al.*[79] Copyright 2014 American Chemical Society. (g) LSV of DRC, Cu NPs/C, and Cu clusters/DRC for the CO_2RR. (h) H_2-TPD curves of DRC, Cu NPs/C, and Cu clusters/DRC. (i) Optimized structural model of Cu(111), Cu_{13}, and Cu_{13}/DG. Adsorption energies of (j) *CO and (k) *H intermediates on the above three models. Reproduced with permission from Alivisatos *et al.*[80] Copyright 2020 Wiley-VCH GmbH.

and Cu foil undergoes structural transformation during the CO_2RR, resulting in an increased nanoparticle size (from 7.0 nm to 23 ± 8 nm) (Fig. 6a and b). Interestingly, even a larger particle with a 52 ± 21 nm diameter is reconstructed into 25 ± 8 nm during the CO_2RR. Furthermore, n-Cu/C displays a CH_4 selectivity of 76%, higher than the FE of 44% on Cu foil (Fig. 6c). Different thicknesses of the Cu film prepared on glass carbon uncover the size effect on catalytic performances, where the evaporated Cu films also undergo a severe structural transformation during the CO_2RR. Isolated nanoscale particles appeared on the thin film (Fig. 6d), while the thick film produced numerous fused nanoparticles (Fig. 6e) under CO_2RR conditions. In contrast, the thin film shows a FE of CH_4 similar to n-Cu/C, and the thick film shows a low FE of CH_4 (Fig. 6f). These studies prove that tiny particles or isolated nanoparticles possess higher activity and selectivity toward CH_4 formation.

Reducing the size of electrocatalysts and keeping it dispersed can affect the binding energy of catalysts to reaction intermediates. Sub-nanometric Cu clusters dispersed on the defective-rich carbon (Cu clusters/DRC) show the highest current density (Fig. 6g) and a maximum FE of 81.7% for CH_4. Reducing the size of catalysts leads to the upshift of the d-band center, thus improving the adsorption intensity of some specific intermediates. To enhance CH_4 selectivity, H species should be fed for the

protonation of *CO rather than for H_2 production. As shown in Fig. 6h, the Cu clusters/DRC offers a board peak in the temperature range of 265–611 °C in the temperature-programmed desorption of H_2 (H_2-TPD) test, indicating the strong adsorption capacity of the H species, which hinders the desorption of *H for H_2 formation. DFT calculations (Fig. 6i) reveal that the adsorption energies of *CO and *H (ΔG_{CO^*} and ΔG_{H^*}) on Cu(111) are much higher than those on the C_{13} clusters and Cu_{13}/DG (Fig. 6j and k). The Cu clusters possess stronger adsorption strength to *CO and *H intermediates, which are the precursors to obtaining the key intermediate of *CHO for CH_4 production. Therefore, it is rational to regard that single metal sites may have better CH_4 selectivity than nanoparticles.

2.3 Coordination number

The catalytic reaction involves the orbital interaction between catalysts and reactants, and thus the coordination number (CN) of catalysts significantly impacts the catalytic performance.[18,66,81–88] The comparative investigation on the relationship between the facet, CN, and product selectivity using DFT calculations shows that CH_4 formation is favorable on the Cu(111) plane and some steps in either direction with a high CN of 9 (Fig. 7a).[89] The products of C_2H_4 and C_2H_5OH tend to form on the plane with a lower CN compared to that of CH_4 (Fig. 7b and c). Similarly, the atomic modeling analysis of the surface atomic CN of spherical Cu nanoparticles demonstrates size-dependent populations of atoms with the CN.[67] When the nanoparticles reduce to

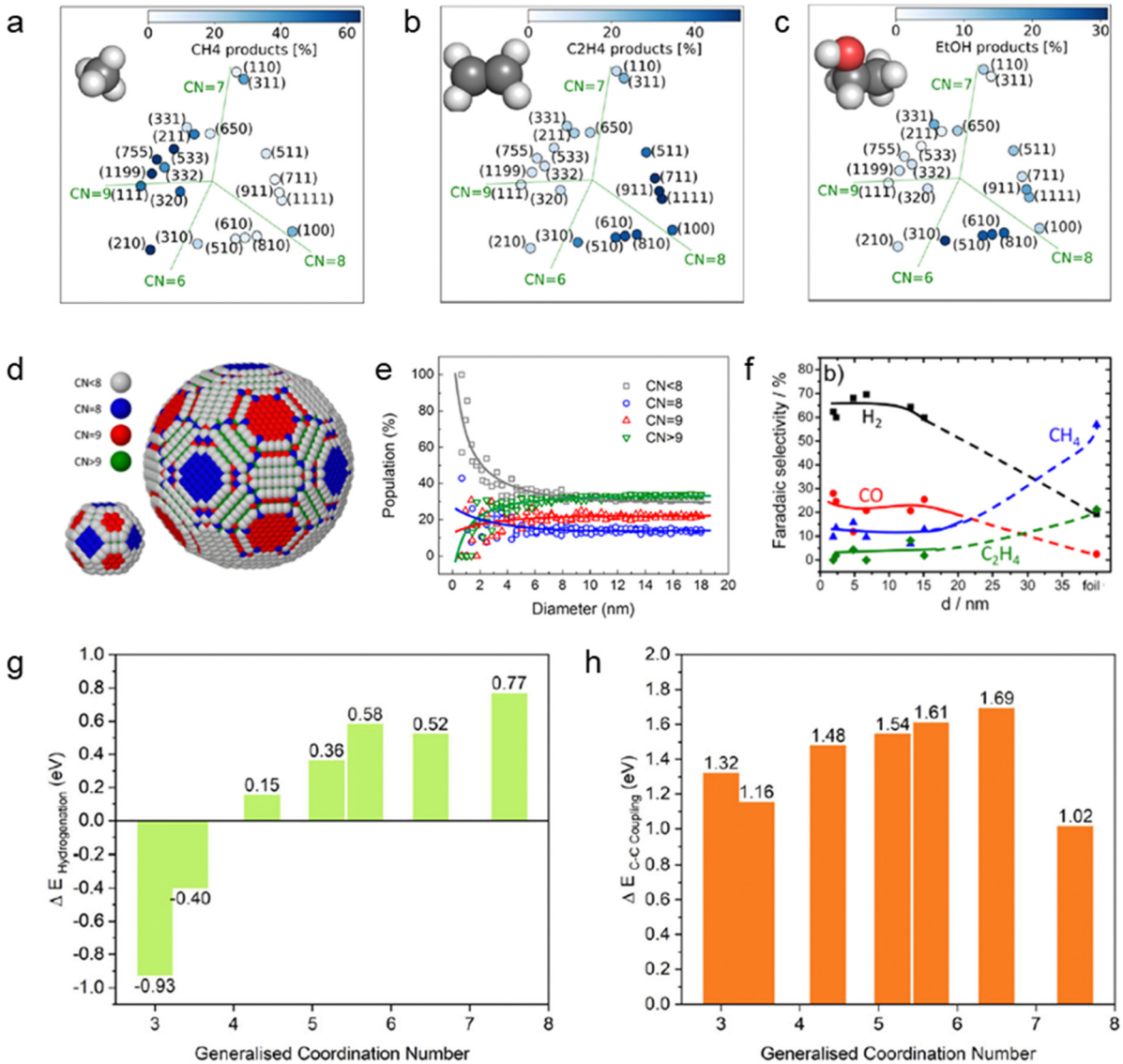

Fig. 7 Principal component analysis of the CN allows for the identification of active sites of the Cu catalyst. (a) Cu(111) gives methane, (b) Cu(100) gives ethylene, and (c) the n(100) × (110) step produces ethanol. Reproduced with permission from Rossmeisl *et al.*[89] Copyright 2019 American Chemical Society. (d) Ball models of spherical Cu NPs with diameters of 2.2 and 6.9 nm. (e) Population (relative ratio) of surface atoms with a specific CN as a function of the particle diameter. (f) The FE of products during the CO_2RR on Cu nanoparticles. Reproduced with permission from Strasser *et al.*[67] Copyright 2014 American Chemical Society. (g) Reaction energies for *CO hydrogenation to *CHO on Cu catalysts of various generalized CNs. (h) Reaction energies for *CO coupling to *OCCO on Cu catalysts of various generalized CNs. Reproduced with permission from Sinton *et al.*[90] Copyright 2021 Springer Nature.

ultrafine size, the low coordinated atoms (CN $\leq$ 9) become dominant, especially the atoms with CN $<$ 8 are drastically augmented below 2 nm (Fig. 7d and e). The contribution of several CNs is relatively even on Cu nanoparticles with a diameter of larger than 10 nm. The electrochemical studies reveal that hydrocarbon products are not favored on nanoparticles less than 15 nm in size. Still, they become increasingly favored as the size grows, which contradicts previous findings by Manthiram *et al.* (Fig. 7f).[79] It might be due to the difference in dispersion between the two Cu nanoparticles and the variable thickness of Cu foil. The FE of CH_4 is slightly increased on the 2–20 nm size regime with a large increase in the CN, indicating the correlation between the FE of CH_4 and the CN of catalysts.

Unlike the above finding, it is found that Cu with a low CN favors CH_4 formation.[32] It is worth mentioning that the calculation models they used to represent low values of atomic coordination are adparticle configurations. The calculated reaction energies reflect that at a CN of 3.0, the formation of the *CHO intermediate (Fig. 7g) is far more favored than the formation of the *OCCO intermediate (Fig. 7h). The variation in the CN has a negligible impact on the C–C coupling process. Thus, the authors believe that low coordination Cu sites can promote CO_2 methanation. They verified this concept by proceeding with the CO_2RR in alkaline electrolytes, not neutral electrolytes, and achieved a FE of 64% for CH_4. Indeed, the CN of active sites greatly influences the performance of CO_2 methanation. As for whether high or low coordination is conducive to methane production, more parameters, such as dispersibility, morphology, and defects, must be considered. As we can see, the CN is related to the facet and the size. Therefore, we should judge the activity of catalysts from many aspects.

2.4 Local pH

The formation of *CHO or *COH from *CO involves the transfer of protons and electrons, the so-called concerted proton–electron transfer (CPET) process.[18] In contrast, *CO dimer formation only involves electron transfer; thus, it depends on the potential, not the pH. The dependence of CH_4 formation on proton activity suggests that CH_4 production is significantly affected by pH and favored in acidic or neutral solutions.[91] However, as the CO_2 reduction is a proton consumption reaction, the OH^- concentration near the electrode surface increases more than the bulk solution, which increases in the local pH.[92] Thus the electrolyte buffer capacity can regulate the local pH to maintain the local proton concentration in electrolytes with high buffer capacities like phosphate, thereby facilitating the selectivity for CH_4 over C_2H_4.[58] In concentrated $KHCO_3$ or phosphate electrolytes, the produced OH^- can be neutralized by adequate HCO_3^- or $H_2PO_4^-$. Although CH_4 production is enhanced with a high local proton concentration, the HER also would be enhanced. Thus, optimizing the adsorption capacity of electrocatalysts to key intermediates should be considered at the same time.

To achieve an industrially relevant current density of the CO_2RR, the alkaline electrolyte is used in a gas-fed flow cell.[93] Using an alkaline electrolyte, C_2H_4 formation is enhanced, while the HER and CH_4 formation is suppressed. Regulating the local pH near the gas diffusion electrode (GDE) is essential for improving CH_4 selectivity at industrially relevant current densities. A pulsed electrolysis method has been introduced to deplete the OH^- species near the electrode surface to enhance the proton concentration.[94] Pulsed electrolysis conditions are set to 1 s pulses at oxidative potentials ranging from E_{an} = 0.6–1.5 V_{RHE}, and the CO_2RR is proceeded at −0.7 V_{RHE} for 1 s. With the increase of E_{an}, the product selectivity shows a remarkable difference (Fig. 8a). At E_{an} values below 1.0 V, the yield of CH_4 is negligible. At E_{an} = –1.0 V, the CH_4 product selectivity surges to 25%, and the maximum CH_4 selectivity of 54% can be obtained at E_{an} = −1.5 V. Raman spectroscopy is a surface-sensitive characterization technique to collect the surface speciation of catalysts (Fig. 8b). At a potential of –0.7 V, a strong band

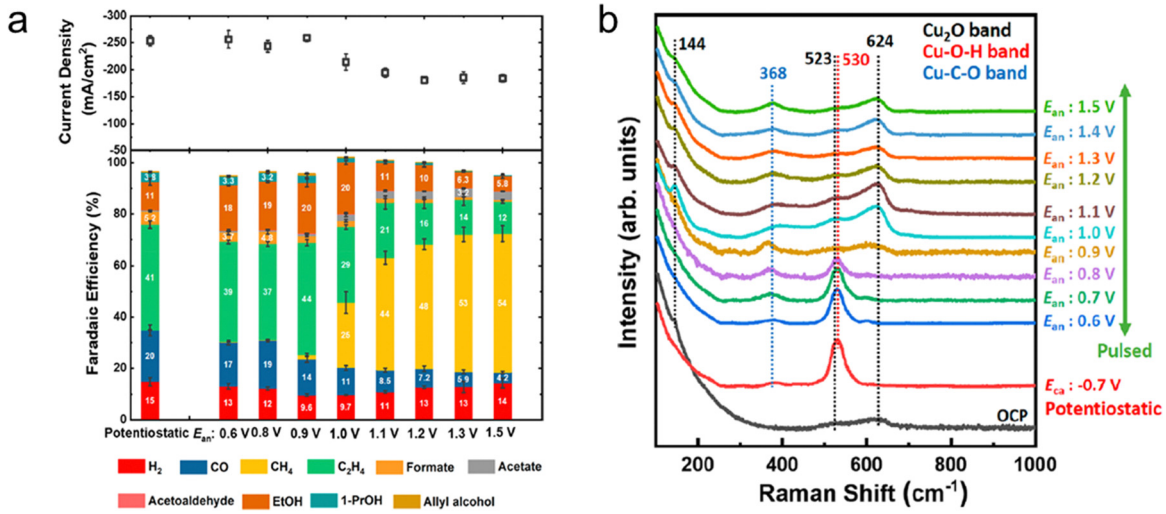

Fig. 8 (a) Current density and FE at −0.7 V using potentiostatic and under pulsed electrolysis conditions with different E_{an} values and the same E_{ca} = −0.7 V cathodic potential in all cases. (b) Operando surface-enhanced Raman spectra under OCP, potentiostatic operation at −0.7 V, and pulsed conditions with different E_{an} values. Reproduced with permission from Cuenya *et al.*[94] Copyright 2021 American Chemical Society.

appeared at 530 cm^{-1}, which is assigned to the Cu–OH signal. Under the pulsed electrolysis conditions, the adsorbed *OH band shows a noticeable decrease with the increase of pulsed potential. The Cu_2O band shows a totally different trend compared to the *OH band, indicating the consumption of OH^- species for Cu_2O formation. The constructed local proton-rich district makes the CH_4 production favorable, achieving a high partial current density of CH_4.

2.5 Cation/anion effect

The cations or anions in electrolytes play an essential role in the electrochemical reaction since they may interact with the electrode surface, reactants, and intermediates and affect the reaction pathway.[66,95,96] The product selectivity of the CO_2RR is greatly affected by cationic or anionic species and their concentration. The cation and anion affect the reaction pathway by regulating the surface potential and local pH.[97–99] It is observed that CH_4 formation increased in the order of $Na^+ > Li^+ > K^+ > Cs^+$, while the C_2H_4 formation is favorable in the order of $Cs^+ > K^+ > Na^+ > Li^+$. Because the smaller cation has a larger hydration number and will not be specifically adsorbed on the electrode surface, the extent of specific adsorption of Li^+ would be the least on the surface and that of Cs^+ the greatest. Specific adsorption of cation shifts the surface potential to the positive direction and lowers the H^+ concentration. The pH at the electrode surface will be lower in the $Cs^+ > K^+ > Na^+ > Li^+$ sequence. We have pointed out that the CH_4 formation is favorable in the region with high proton activity. Therefore, the FE of CH_4 is higher in Li^+ and Na^+ solutions, with the Na^+ solution being more favorable than the Li^+ solution. However, the HER also proceeds in a high H^+ concentration solution simultaneously.

Furthermore, the anions can also affect the local pH by their buffer capacity. The formation of CO, $HCOO^-$, C_2H_4, and CH_3CH_2OH is little affected by the composition and concentration of anions because the rate-limiting step of these products does not involve H^+.[100] Thus, the anion mainly affects the formation of H_2 and CH_4. Apart from the local pH, anions can affect the surface electronic structure of electrocatalysts; for instance, the halide anions could regulate the catalyst surface electronic structure and thus optimize the reaction pathway.[99] When I^- is introduced into the electrolyte, it adsorbs on the Cu surface and donates electrons to Cu, resulting in a negatively charged surface. The interaction between the negatively charged Cu surface and the partially positively charged carbon atom of CO_2 and CO is enhanced (Fig. 9a), resulting in the enhancement of CO_2 methanation (Fig. 9b). Therefore, it is obvious that the cation/anion affect the electrochemical properties mainly by regulating the local environment of electrodes and the electrolyte.

2.6 CO concentration

It is important to go through the *CO intermediate phase when producing CH_4 or other C_2 compounds. As a result, it stands to reason that the CO concentration influences the reaction pathway and product selectivity.[37,103–105] Besides, the *CO dimerization and HER should be suppressed to improve CH_4 selectivity

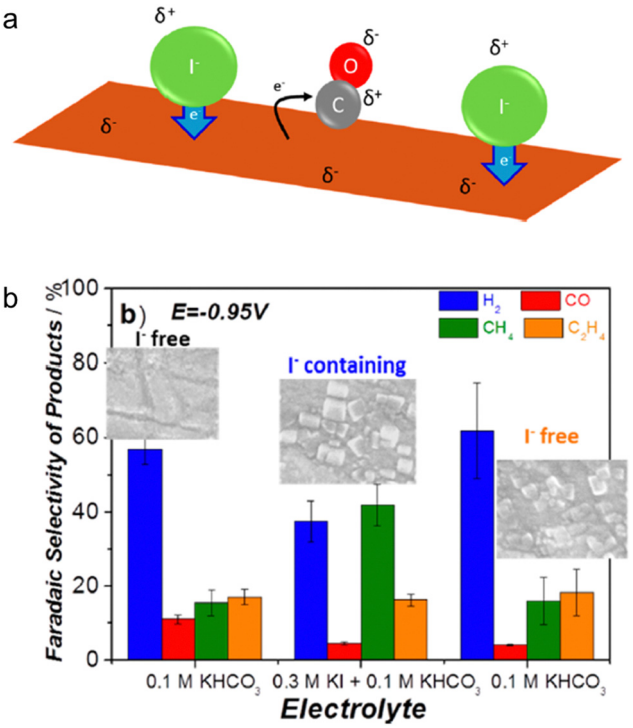

Fig. 9 (a) Scheme illustrating how the presence of I^- affects the net charge of Cu, making it more negative and facilitating the charge transfer for CO reduction. (b) Faradaic selectivity of the gaseous products after 10 min of bulk electrolysis at a constant potential of 0.95 V *vs.* RHE. Including the SEM images of the surface after the reaction. Reproduced with permission from Strasser *et al.*[99] Copyright 2016 American Chemical Society.

by lowering the surface *CO coverage.[105] DFT studies provide insights into free energies of *CO to *CHO (ΔG_{*CHO}) and C–C coupling (ΔG_{*OCCOH}) for CH_4 production and C_2 products under different *CO coverages to figure out the surface *CO coverage (Fig. 10a). According to free energy calculations, when the *CO coverage is reduced from the 4/9 to 3/9 monolayer the values of ΔG_{*CHO}–ΔG_{*OCCOH} on Cu and Au–Cu surfaces decrease, which implies that low *CO coverage promotes CH_4 production (Fig. 10b). However, using the square-wave potential electrolysis method, after flipping the electrode at a higher frequency, the *CO concentration on the Ag–Cu electrode surface increased, which enhanced the CH_4 selectivity (Fig. 10c).[104] One consensus is that introducing a CO-producing material on Cu can promote CH_4 production, but the improved local CO concentration can also promote C_2H_4 generation.[106] Therefore, the *CO concentration cannot be directly correlated with CH_4 product selectivity.

3. Advanced single site electrocatalysts towards CO_2 methanation

It is well known that Cu-based catalysts efficiently convert CO_2 into multi-carbon products through the C–C coupling pathway. However, when active sites are reduced to single isolated sites, C–C coupling is inhibited because the two *CO intermediates

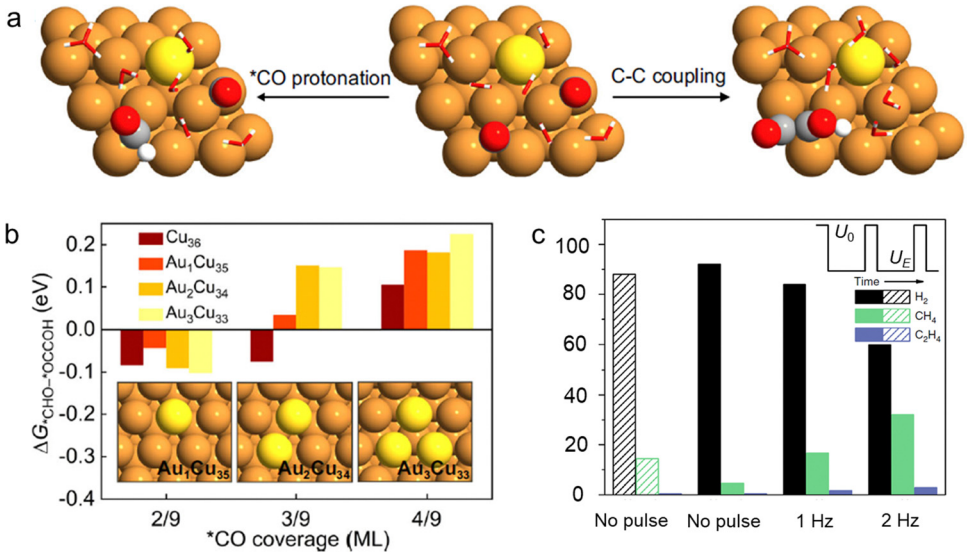

Fig. 10 (a) Geometries of *CO, *CHO, and *OCCOH intermediates on the Au–Cu surface. (b) Reaction free energy difference between *CO protonation and C–C coupling steps on Cu_{36}, Au_1Cu_{35}, Au_2Cu_{34}, and Au_3Cu_{33} surfaces at different *CO coverages. Reproduced with permission from Sargent *et al.*[101] Copyright 2021 Springer Nature. (c) Faradaic efficiencies of CO electroreduction products with and without square-wave potential electrolysis. Reproduced with permission from Lu *et al.*[102] Copyright 2019 Springer Nature.

Table 1 Summary of the major SSCs toward methane

Types	Catalysts	Electrolytes	FE (CH_4)	Current density (CH_4)	Ref.
Molecular SSCs	Cu(I)-based polymer NNU-33 (H)	1 M KOH	82%	391.79 mA cm^{-2}	34
	$Cu_4ZnCl_4(btdd)_3$	0.5 M $NaHCO_3$	88%	18.3 mA cm^{-2}	48
	Cu-TDPP-NS	0.5 M PBS	70%	183 mA cm^{-2}	35
	Cu-DBC	1 M KOH	80%	162.4 mA cm^{-2}	36
	Cu-Tph-COF-Dct	1 M KOH	80%	220 mA cm^{-2}	37
	2Bn-Cu@UiO-67	1 M KOH	81%	340.2 mA cm^{-2}	38
	Plasma activated CuDBC	0.5 M $NaHCO_3$	75.3%	36 mA cm^{-2}	107
	NC-SA Cu/COF	0.1 M $NaHCO_3$	56.2%	4.2 mA cm^{-2}	108
Carbon-supported SSCs	CoPc@Zn-N-C	1 M KOH	18.3%	44.3 mA cm^{-2}	109
	CuN_2O_2	0.5 M $NaHCO_3$	78%	31.2 mA cm^{-2}	47
	Cu SAs/GDY	1 M KOH	81%	243 mA cm^{-2}	39
	Cu SA/F-GDY	1 M KOH	72.3%	174.24 mA cm^{-2}	110
Oxide-supported SSCs	Cu–CeO_2-4%	0.1 M $NaHCO_3$	58%	~36 mA cm^{-2}	111
	Cu/p-Al_2O_3 SAC	1 M KOH	62%	94.8 mA cm^{-2}	46
	Cu/CeO_2	0.1 M $NaHCO_3$	49.3%	~8 mA cm^{-2}	112
	Ir_1–Cu_3N/Cu_2O NCs	1 M KOH	75%	240 mA cm^{-2}	113

utilized for C–C coupling are located on two active sites. Thus, C_1 compounds like CO, CH_3OH, and CH_4 are the main products of SSCs. To obtain the CH_3OH or CH_4 product, the adsorption of *CO on active sites should be stronger enough so that *CO can be further reduced and hydrogenated. The coordination structure directly determines the electronic structure of the active site, which is essential for the adsorption capacity of SSCs to reaction intermediates. In this section, we review the recent advances of SSCs for CO_2 methanation and highlight the coordination structure regulation and reaction mechanism analysis (Table 1).

3.1 Molecular catalysts

In the early 1980s, nickel and cobalt macrocyclic compounds were reported to convert CO_2 into CO.[114] Later on, the application of a series of metal phthalocyanines was explored for the CO_2RR and it found that CO is the only product on Co and Ni phthalocyanines.[115] Meanwhile, formic acid was dominant on Sn, Pd, and In phthalocyanines, methane was the main product on Cu, Ga, and Ti phthalocyanines. However, molecular catalysts were ignored for decades and applied to the CO_2RR recently. A molecular catalyst is a typical SSC that plays an important role in homogeneous and heterogeneous catalysis due to its well-defined and tunable structure.

CO_2 activation is also a decisive step for molecular catalysts to initiate the CO_2RR. Because of competing processes such as the HER, protons compete with CO_2 for the active site. According to reports, Co^{2+} in Co protoporphyrin would take an electron to become Co^+ and then mix with CO_2 to form M-(CO_2^-), a Brønsted base capable of attracting protons from water (Fig. 11a).[33] The CO_2 activation capacity is linked to the Co^{2+}/Co^+ redox potential; the closer the Co^{2+}/Co^+ redox

potential is to the overall equilibrium potential, the smaller the overpotential for CO_2 reduction. However, due to the weak adsorption ability to *CO, the main product of Co protoporphyrin is CO. Thus, a more acidic environment or stronger CO_2/CO adsorption is necessary to reduce the *CO further for a higher CH_4 yield. An N-heterocyclic carbene (NHC)-ligated Cu single atom sites embedded into a metal–organic framework (2 Bn-Cu@UiO-67) shows optimized adsorption of *CHO intermediates on the increased charge density of Cu sites due to the electron donor effect of NHC ligands (Fig. 11b and c).[38] Moreover, the porous structure of UiO-67 facilitates the diffusion of CO_2 and enhances mass transfer, yielding a FE of 81% for CH_4 at a high current density of 420 mA cm^{-2} (Fig. 11d and e). Thus, it is evident that a strong adsorption capacity of a single metal site is essential for further reduction of *CO to CH_4.

Like Co protoporphyrin, Cu^+ also substantially affects CO_2 activation and product selectivity in Cu-based molecules. The activity and selectivity of the CO_2RR have been demonstrated to be significantly impacted by Cu^+ in Cu oxides, although Cu^+ cannot be stabilized in oxides and soon reduces to Cu^0.[117] Benefiting from the robust ligand structure, molecular catalysts can stabilize the Cu^+ active site, where Cu would transform from Cu^{2+} to Cu^0. In a non-planar structure molecule, Cu^+ can be stabilized by strong trigonal pyramidal coordination (Fig. 12a). Under CO_2RR conditions, the Cu^{2+} sites are reduced to Cu^+ active sites and stabilize at a high-negative potential (Fig. 12b). Besides, the second coordinate sphere can also stabilize the *CHO intermediates by adjacent aromatic hydrogen atoms, promoting the production of CH_4. For planar structural molecules, introducing coprophilic interactions (Cu–Cu distance in the range of 2.4–3.0 Å) is a feasible strategy to stabilize Cu^+ sites. A Cu^+-based coordination polymer electrocatalyst (NNU-32) with abundant coprophilic sites demonstrated excellent ability of CO_2 to CH_4 conversion.[34] If a sulfate group is introduced into the molecule (NNU-32(S)), the sulfate group will be replaced by a hydroxyl radical (NNU-32(H)) in the alkaline electrolyte (Fig. 12c). The substitution of hydroxyl radicals for sulfate radicals results in enhanced coprophilic interactions and thus further improves the CH_4 product selectivity to 82% at −0.9 V *vs.* RHE.

When designing the coordination structure, it is also necessary to consider the spatial potential resistance effect. The reaction pathway and product selectivity can be successfully modified by varying the size of the second coordination sphere layer ligand. Cu(I) triazolate frameworks with three ligand side groups (MAF-2ME, MAF-2E, and MAF-2P) have been developed, where the steric hindrance prevents the combination of two *CO intermediates as the size of the ligand side groups increases (Fig. 12d).[118] Thus, MAF-2P is difficult to distort to bind the second CO intermediate for producing C_2H_4 (Fig. 12e). The C_2H_4/CH_4 selectivity ratio can be adjusted from 11.8 : 1 to 1 : 2.6 with an increase in the size of ligand side groups.

3.2 Carbon-supported catalysts

Carbon-supported metal single atom catalysts (CS-SACs) have emerged as promising electrocatalysts for the CO_2RR. Unlike the single molecular unit of molecule catalysts, CS-SACs have continuous carbon networks with metal atoms embedded in the network, meaning that the coordination structure optimization focuses on the first coordination shell. Metal–N_4–C is a typical structure in CS-SACs, whereas single metal sites possess high stability due to the strong binding strength of N to metal atoms. Cu-based catalysts bear strong adsorption to *CO, so Cu-based SACs attract the most attention. To inhibit the possible *CO dimerization, the distance between the neighboring Cu–N_x species should be far enough. At a high Cu atom concentration, the distance of two Cu–N_x species was too close to trigger *CO dimerization (Fig. 13a), and a low Cu atom concentration ensured the high dispersion of Cu–N_x species, favoring the formation of CH_4.[119] At a Cu concentration lower than 2.4 mol%, a CH_4 FE of 38.6% can be achieved.

Due to possible *CO dimerization on Cu-based SACs, Cu-free SACs are sought for efficient CO_2 conversion into hydrocarbons

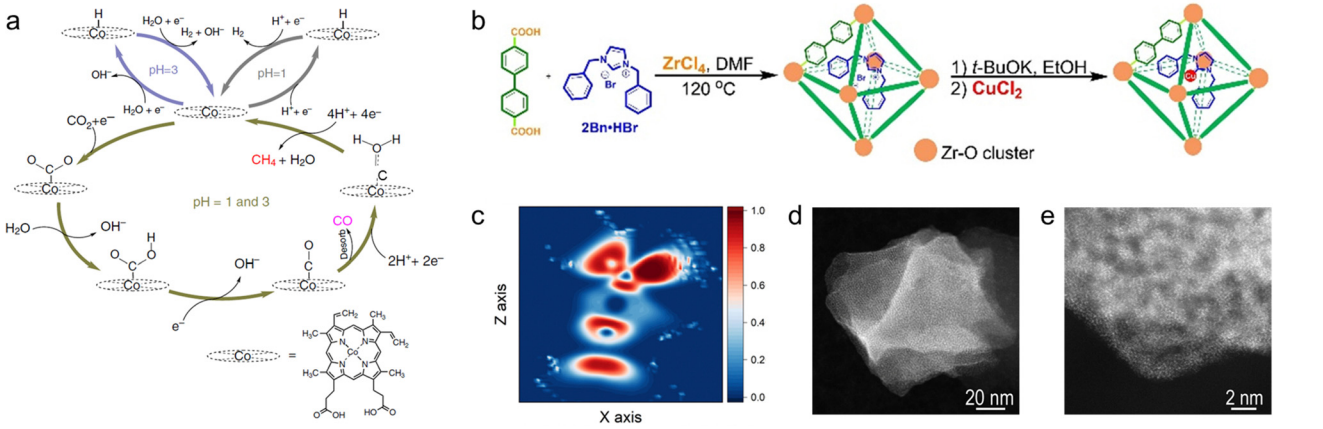

Fig. 11 (a) Proposed mechanistic scheme for the electrochemical reduction of CO_2 on Co protoporphyrin. Reproduced with permission from Koper *et al.*[116] Copyright 2015 Springer Nature. (b) The schematic of the synthesis process for 2 Bn-Cu@UiO-67. (c) The electron localization function of 2Bn-Cu@UiO-67 with the adsorption of *CHO (d) and (e) HAADF-STEM of 2Bn-Cu@UiO-67. Reproduced with permission from Li *et al.*[38] Copyright 2021 Wiley-VCH GmbH.

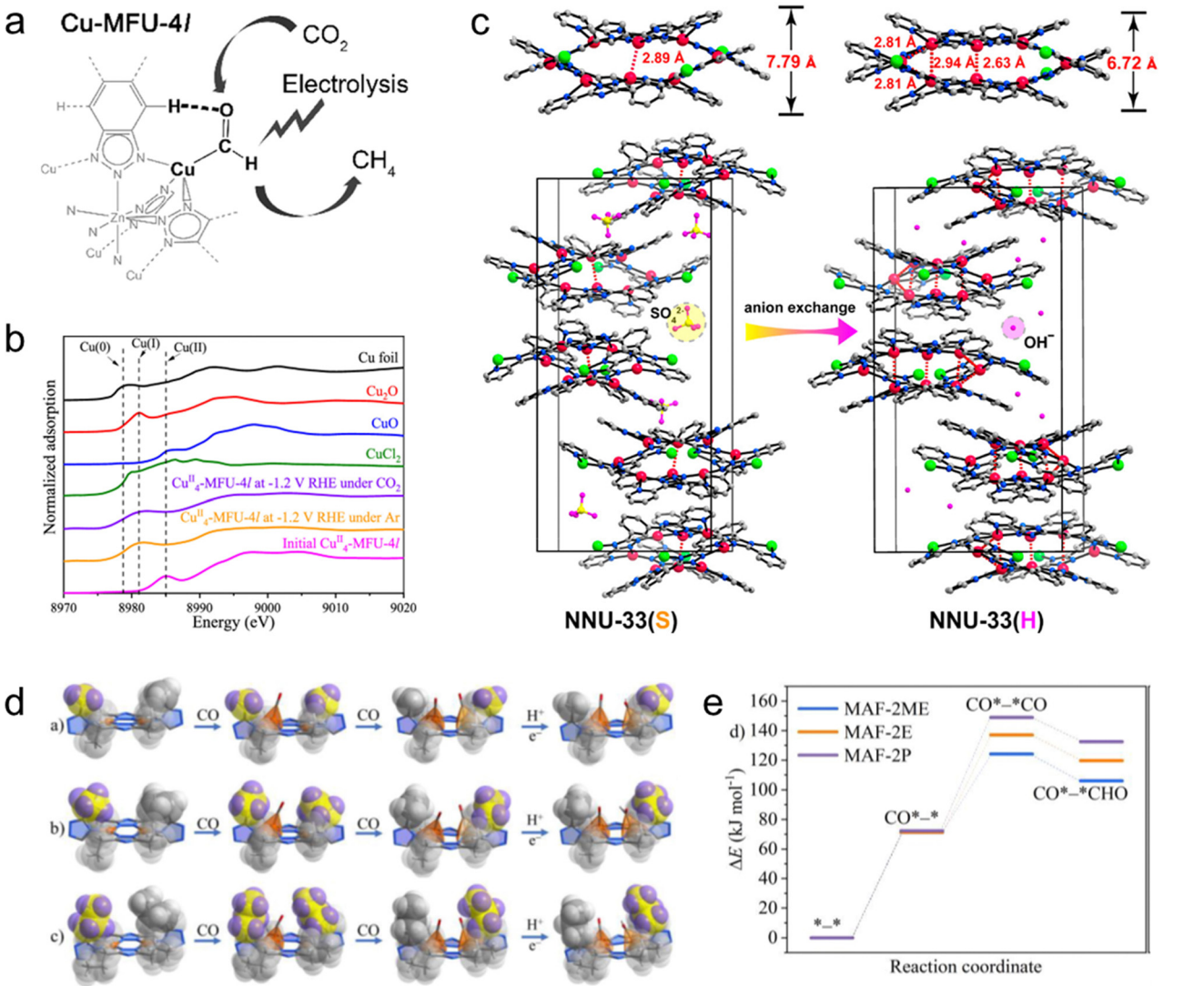

Fig. 12 (a) The schematic of the CO_2RR mechanism on Cu-MFU-4l. (b) Normalized Cu K-edge XANES spectra of Cu-based samples. Reproduced with permission from Lan *et al.*[48] Copyright 2021 American Chemical Society. (c) The structures of {Cu_8} clusters and unit cells in NNU-33(S) and NNU-33(H), respectively. Reproduced with permission from Chen *et al.*[34] Copyright 2021 American Chemical Society. (d) Periodic density functional theory-derived structures of the CO_2RR intermediates for MAF-2ME, MAF-2E, and MAF-2P. (e) Reaction free energies of CO_2RR on MAF-2ME/MAF-2E/MAF-2P. Reproduced with permission from Zhang *et al.*[118] Copyright 2022 Wiley-VCH GmbH.

and oxygenates. Cu-free SACs such as Fe–N_x sites typically convert CO_2, CO, and CH_2O into CH_4 with a low FE due to the low intrinsic adsorption capacity to *CO with the major product CO (Fig. 13b).[120] Introducing an axial oxygen atom on M–N_4–C catalysts can change the electronic structure of center metal atoms and affect the adsorption strength of intermediate species.[121] Considering the number of d-electrons and electronegativity, five SACs (Mn–N_4–C, Cr–N_4–C, Os–N_4O–C, Ru–N_4O–C, and Rh–N_4O–C) close to the summit of the volcano-shaped relationships between the activity descriptor and limiting potentials. However the five-coordination structure is not quite stable. Constructing an oxygen-containing four coordination structure can also promote the further reduction of *CO. A unique Cu–N_2O_2 structure was reported for CO_2 conversion to CH_4 with high selectivity (Fig. 13c).[47] On Cu–N_2O_2 sites, the overall endothermic energy of intermediates for *COOH and *COH is lower than that of CuN_4 but still higher than that of Cu(111). The enhanced CH_4 selectivity originated from the higher formation energy of *H adsorption on CuN_2O_2 than that of CuN_4 and Cu(111) because of the optimizing electronic structure (Fig. 13d). Besides, constructing tandem catalysts is also a feasible pathway to achieve high CH_4 selectivity on Cu-free SACs. Cobalt phthalocyanine (CoPc) is a typical CO-selective catalyst.[122] A CoPc-ZnNC tandem catalyst improves the CH_4/CO production rate ratio by 100 times, with CO_2 first reduced to CO on CoPc sites, and then diffused CO reduced to CH_4 through the Langmuir–Hinshelwood route including an adsorbed *H on Zn sites (Fig. 13e). It provides an alternative strategy for the possible *CO dimerization in CO_2 methanation.

Graphdiyne (GDY) is a unique platform for anchoring single atoms with M–C bonds. The –C≡C–C≡C structure in GDY

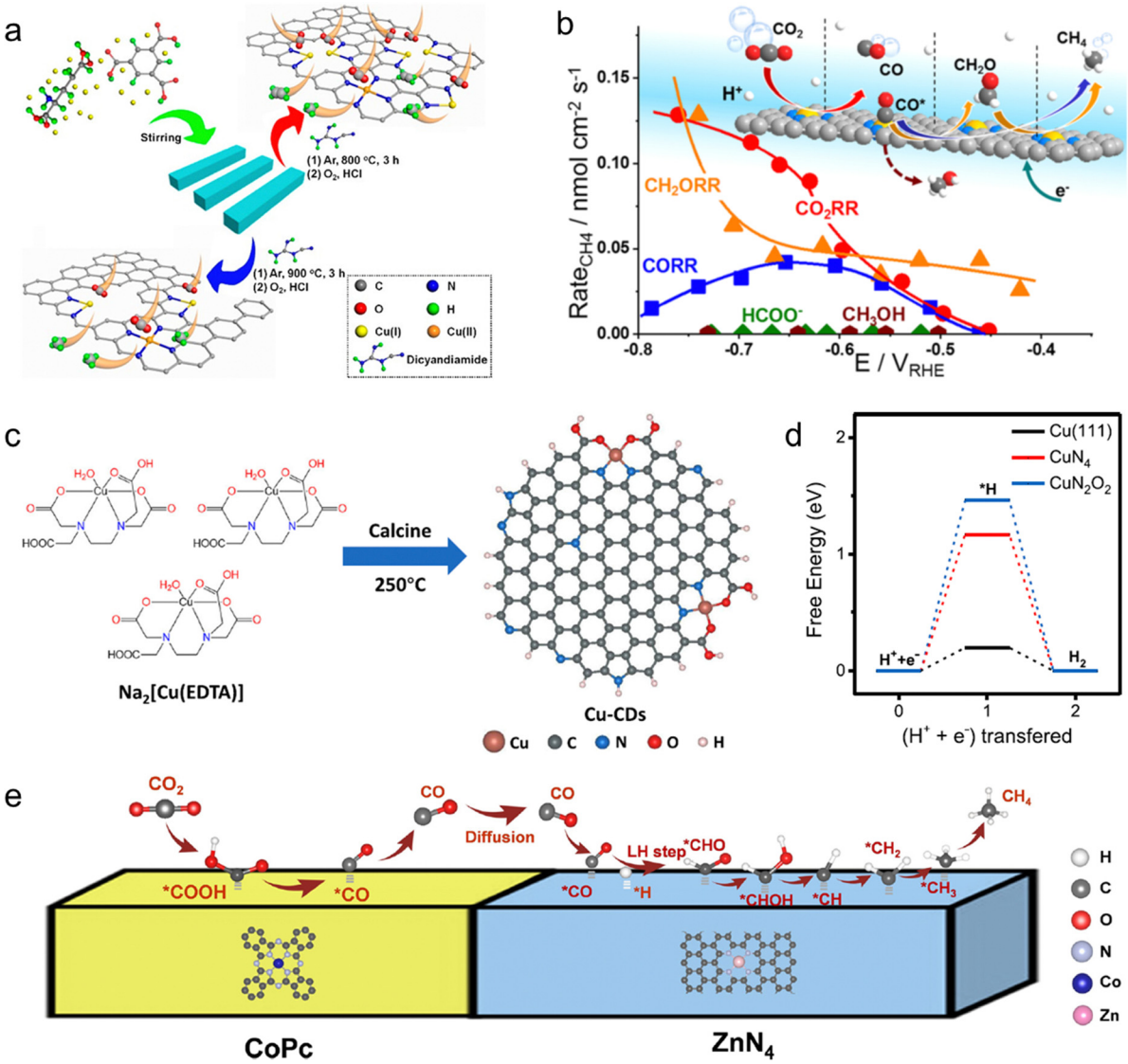

Fig. 13 (a) Schematic of the synthesis of the Cu–N–C–T catalysts. (b) Catalytic methane production rate on Fe–N–C during the electrochemical reduction of CO_2, CO, and CH_2O. Reproduced with permission from Strasser *et al.*[120] Copyright 2019 American Chemical Society. (c) Scheme of the synthesis of Cu-CD ($Cu–N_2O_2$) catalysts. (d) Free energy diagram of hydrogen evolution on CuN_2O_2, CuN_4, and Cu(111). Reproduced with permission from Zhu *et al.*[123] Copyright 2021 Springer Nature. (e) The proposed reaction mechanism of the CO_2RR to CH_4 over CoPc@ZnNC. Reproduced with permission from Wang *et al.*[109] Copyright 2020 Wiley-VCH GmbH.

can stabilize single atoms and trigger electron transfer between the metal center and GDY.[124,125] On the Cu-based SAC-GDY system, CO_2 methanation may be more easily carried out *via* the *OCHO pathway to avoid *CO dimerization.[39] The orbital hybridization between the Cu atom and graphite alkyne regulates the electronic structure of the Cu atom, promoting the valence state of the Cu atom higher than 0. The Cu–C bond also changes the $*CO_2$ protonation state to *OCHO, which enhances the CH_4 product selectivity.

3.3 Oxide-supported catalysts

Due to the nature of the vacancy-prone and strong metal–support interactions, metal oxides are widely used to support atomically dispersed metal atoms.[126,127] Defect-rich metal oxides have strong anchoring capability to metal atoms, which can inhibit the aggregation of metal atoms and *CO dimerization. CeO_2 is known to generate strong metal–support interactions. Au–CeO_x and Ag–CeO_x have shown higher CO FE due to the interface-enhanced effect.[128] Coupling single-atomic Cu substitution and multivacancy can effectively improve CH_4 selectivity.[111] From theoretical prediction, the structure of three oxygen vacancy (V_O) neighbors to the doped Cu atom is the most stable structure (Fig. 14a). Specifically, the valence state of Cu atoms is reduced to Cu^+ with three V_O, which is more suitable for CH_4 production. The adsorbed CO_2 can be stabilized in a bent structure on the Cu-3V_O site while in a linear structure on other vacancy structures or undoped CeO_2. The CO_2 adsorption energy of the former structure is −0.39 eV,

significantly promoting the CH_4 formation process. As mentioned earlier, a high local proton concentration is beneficial for CO_2 methanation. Apart from the free protons in electrolytes, the Lewis acid–base interactions can also facilitate the stabilization of the *HCOO intermediate and CH_4 formation. Chen *et al.*[46] found that loading a Cu single atom on strong Lewis acid Al_2O_3 and weak Lewis acid Cr_2O_3 can improve CH_4 selectivity. On the strong Lewis acid Al_2O_3 substrate, the formation energy of *HCOO is only −0.25 eV, far lower than *COOH, and the proton–electron transfer of $*CH_3O$ prefers to produce CH_4 over CH_3OH because of a lower free energy increase, which reveals that the CH_4 pathway proceeds preferentially over CO and CH_3OH pathways (Fig. 14b). When Cu single atoms are loaded on the weak Lewis acid Cr_2O_3, the formation of *HCOO is strongly endothermic (Fig. 14c). Therefore, the increase of CH_4 formation on Cu/Cr_2O_3 is limited. Benefiting from the strong Lewis acid–base interaction, a high FE of 62% toward CH_4 can be achieved on Cu/Al_2O_3.

In addition to being a reaction active site, metal single atoms can also act as co-catalysts. Chen *et al.*[113] designed an

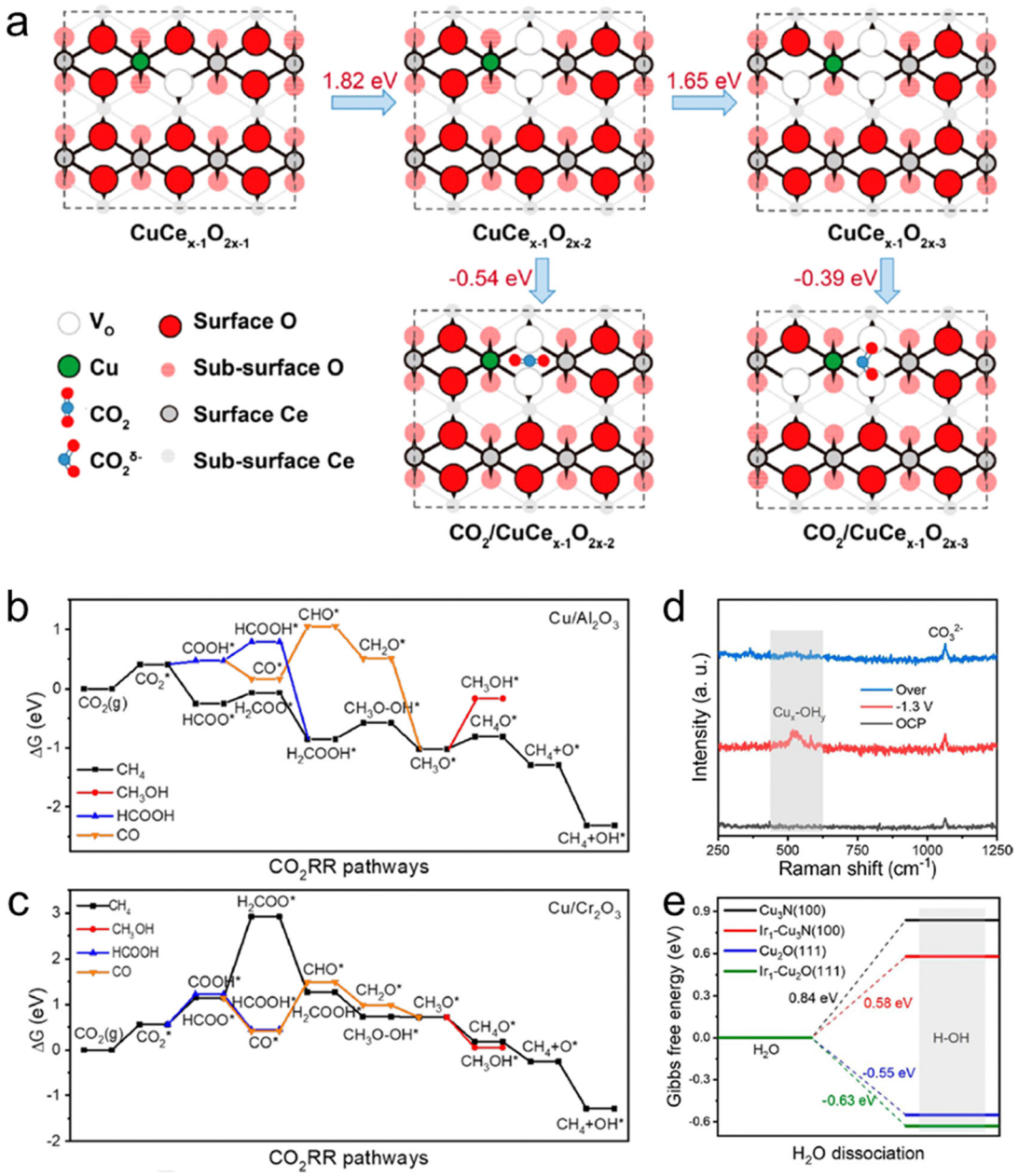

Fig. 14 (a) Theoretical calculations of the most stable structures of Cu-doped CeO_2(110) with vacancies and their effects on CO_2 activation. Reproduced with permission from Zheng *et al.*[111] Copyright 2018 American Chemical Society. Calculated free-energy diagrams for the CO_2RR over (b) Cu/Al_2O_3 SACs and (c) Cu/Cr_2O_3 SACs. Reproduced with permission from Li *et al.*[46] Copyright 2021 American Chemical Society. (d) *In situ* Raman spectrum of Ir1–Cu_3N/Cu_2O. (e) Calculated free energy change for the water dissociation process of Cu_3N(100) and Ir_1–Cu_3N(100) and Cu_2O(111) and Ir_1–Cu_2O(111). Reproduced with permission from Li *et al.*[113] Copyright 2022 American Chemical Society.

iridium single-atom doped Cu_3N/Cu_2O hybrid catalysts (Ir_1–Cu_3N/Cu_2O). The Ir_1 is capable of water dissociation to produce H^+ and OH^-. As shown in the results of *in situ* Raman (Fig. 14d), the Cu_x–OH_y species exist on Ir_1–Cu_3N/Cu_2O when the potential is applied, while it is significantly weak on Cu_3N, indicating the enhancement of water dissociation by introducing Ir_1 atoms. Moreover, the free energy change of Ir_1–$Cu_3N(100)$ (0.58 eV) and Ir_1–$Cu_2O(111)$ (−0.63 eV) for water dissociation delivers smaller absolute values than those of pure $Cu_3N(100)$ (0.84 eV) and $Cu_2O(111)$ (−0.55 eV), further verifying the acceleration of water dissociation by Ir_1 (Fig. 14e). Ir_1–Cu_3N/Cu_2O catalysts achieve a high FE of 75% for CH_4 in alkaline flow cells, which is usually unfavorable for CH_4 production. It highlights the importance of designing local coordination environments around active sites. It is worth noting that up to now, most reports on oxide-supported SACs for CO_2 methanation are based on Cu sites because of the strong adsorption of Cu sites to the *CO intermediate. Therefore, more extensive investigations are required for CO_2 methanation on Cu-free oxide-supported SACs.

4. *In situ* characterization methods for tracing single active sites

At the high negative applied potential of the CO_2RR, most metal compounds will undergo a decrease in the valence state of the metal ion and a drastic change in the morphology and structure.[113,129–132] Also, SSCs will undergo obvious changes in the valence state of metal ions, and even restore to zero valences to obtain metal particles or clusters.[133] However, the content of metal atoms in SSCs is usually less than 10 wt%, so it is challenging to trace the structural variation of metal sites during the CO_2RR. Thus, *in situ* characterization studies are crucial for investigating the structural changes of single-site electrocatalysts during CO_2 methanation. These characterization studies enable the identification of the active sites and reaction intermediates, as well as the determination of the mechanisms of the catalytic reactions. *In situ* techniques such as X-ray absorption spectroscopy (XAS), Raman spectroscopy, infrared spectroscopy, and UV-visible spectroscopy, among others, are particularly useful in this regard.[134] By monitoring the changes in the electrocatalyst structure and composition during the reaction, *in situ* characterization studies provide insights into the reaction mechanism and help optimize the electrocatalytic performance for CO_2 reduction.

4.1 *In situ* XAS

In situ XAS is a powerful technique used to study the structural changes of materials under electrochemical conditions.[90,133,135–137] It involves using synchrotron radiation to probe the electronic and geometric structure of materials. By analyzing the X-ray absorption spectra of the catalyst in real-time during an electrochemical reaction, the oxidation state, coordination geometry, and local environment of the active site of the catalyst can be clearly revealed. XAS encompasses two main methods: X-ray absorption near edge structure (XANES) and extended X-ray absorption fine structure (EXAFS).[138] XANES is a method that provides information on the electronic structure and reveals details about the oxidation state and coordination environment of the atoms in the material. EXAFS, on the other hand, is a technique that provides information on the geometric structure of a material and provides information on the bond distances, coordination numbers, and disorder in a material's structure. In the realm of SSCs, which often contain ultralow amounts of metal, *in situ* XAS is a highly effective method for investigating changes in the valence state and coordination structure of the catalyst during electrochemical reactions.

SSCs are typically coordinated to non-metal atoms, most commonly nitrogen atoms, resulting in a tightly bound structure that imparts exceptional stability to these catalysts. However, despite the robust nature of the M–N bonds in SSCs, they can still be disrupted under the extremely high negative pressure of the CO_2RR. It has been found that when a single Fe atom exists on Cu(111), it exhibits the strongest affinity for *CO over competing *H and the lowest hydrogenation energy of *CO, indicating a propensity for the CO_2RR to produce methane (Fig. 15a).[135] As the size of the Fe unit increases from single atoms to nanoparticles, the selectivity of CO_2RR products decreases, while that of H_2 increases, owing to the highest affinity of single-site Fe for *CO over *H. Preventing the aggregation of single-site Fe during the CO_2RR is crucial. Fe single atoms in Fe phthalocyanine (FePc) are well-isolated, with a significant distance between two Fe single atoms. The Fe single atom can be maintained by anchoring FePc units onto Cu(111) even if Fe^{2+} is reduced to Fe^0. Through *in situ* XAS analysis, it has been discovered that during the CO_2RR, the Fe–N bond dissociates, and a Fe–Cu metallic bond emerges, with a lower coordination intensity than pure Fe metal (Fig. 15b). As a result, the oxidation state shifts from a cation to a metallic state, and the electronic state differs from that of pure Fe metal (Fig. 15c). The significant diameter of the phthalocyanine ring (15 Å) effectively isolates iron ions (2.52 Å) and prevents the self-aggregation of Fe ions.

Cu–N based SCCs are the most common catalysts for CO_2 methanation. However, it is reported that a Cu–N–C material composed of predominantly Cu–N sites can catalyze CO_2 into ethanol with high faradaic efficiency.[136,139] As we all know, the formation of the C_2 product involves two *CO intermediates on two active sites nearby and the large interatomic distances of single sites would not allow this process to occur (Fig. 15d).[140] Therefore, when C_2 products are observed, cluster formation is highly probable. Using *ex situ* characterization methods such as X-ray photoelectron spectroscopy (XPS) and high-angle annular darkfield scanning transmission electron microscopy (HAADF-STEM), it is found that Cu–N_4 motifs can be maintained post-electrolysis, which prompted us to consider whether there is a different reaction mechanism. However, *in situ* XAS showed that Cu^{2+} reduction to Cu^0 and Cu–Cu coordination showed up below −0.6 V *vs.* RHE, indicating the formation of Cu clusters during CO_2 electrolysis. Interestingly, after exposure to air for 10 hours or applying a positive potential of +1 V *vs.* RHE, Cu–Cu coordination disappeared while the original Cu–N coordination recovered. These results suggest that the Cu_n clusters produced

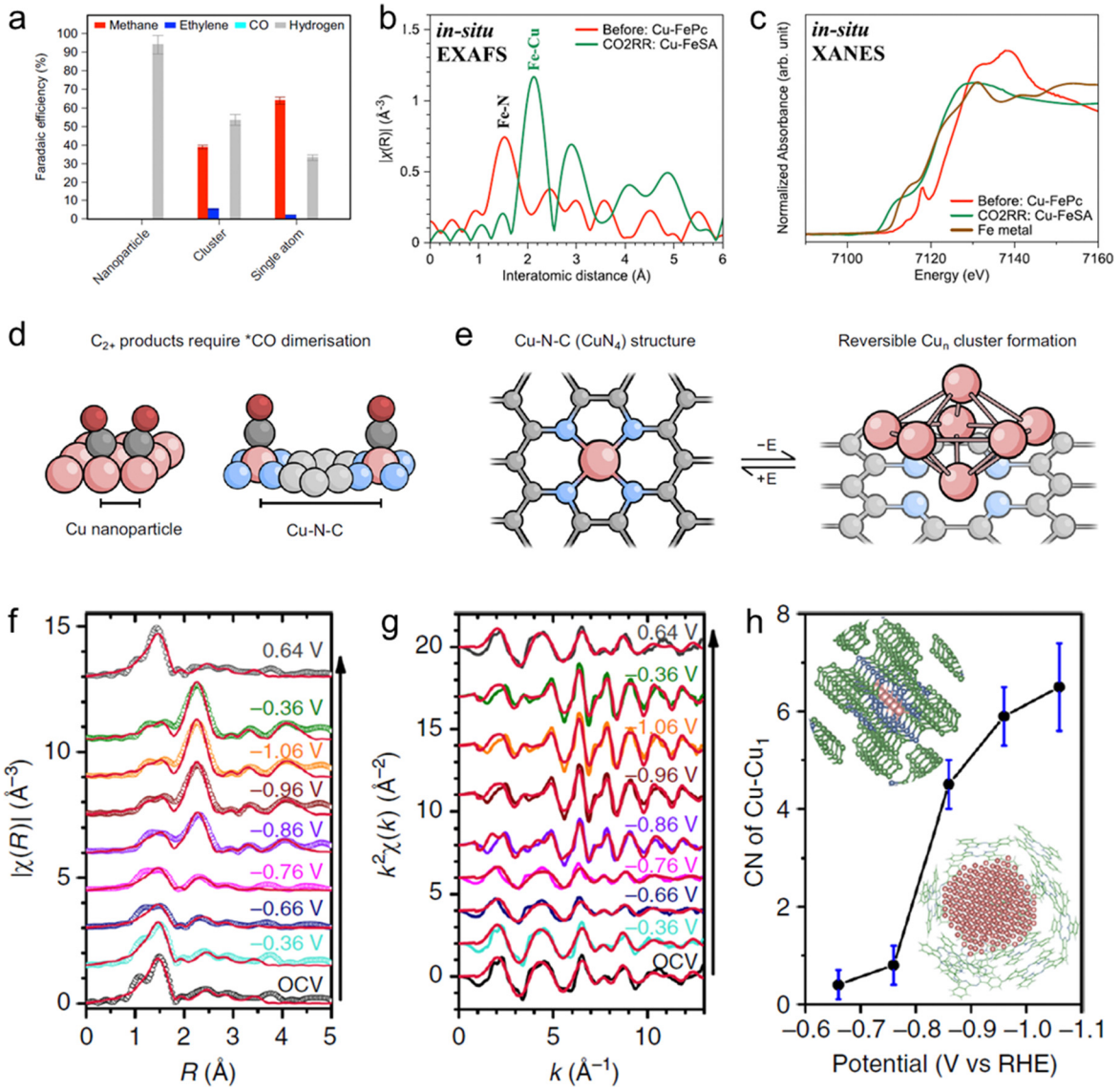

Fig. 15 (a) The FE of CH_4 on various iron-dispersed copper materials, including nanoparticle, cluster, and single-atom forms. (b) *In situ* EXAFS and (c) XANES of Fe K-edge for Cu-FeSA during the CO_2RR. Reproduced with permission from Sargent *et al.*[135] Copyright 2022 Springer Nature. (d) Illustration of how Cu–Cu distances affect *CO dimerization. (e) Schematic showing the formation of Cu_n clusters at an applied cathodic potential and the reversibility at oxidative potentials. Reproduced with permission from Fontecave *et al.*[140] Copyright 2022 Springer Nature. Fitted (f) *R*-space and (g) *k*-space EXAFS spectra of the CuPc catalyst. (h) First-shell Cu–Cu CNs of the CuPc catalyst at different potentials. Reproduced with permission from Wang *et al.*[133] Copyright 2018 Springer Nature.

during electrolysis are responsible for ethanol production and the Cu–N structure can be recovered with the oxidation of Cu^0 because the undercoordinated N sites still exist, which would capture the metal ions (Fig. 15e). Different Cu single site coordination structures are transformed into clusters of various sizes during the CO_2RR, which significantly impacts the regeneration of their structures. A typical Cu-based molecular catalyst, copper(II) phthalocyanine (CuPc), reversibly restructures to Cu clusters with a size of ~2 nm upon application and release of the negative electrode potential.[133] In contrast, in a Cu–O coordinated metal–organic framework (MOF), copper(II) benzene-1,3,5-tricarboxylate (btc) MOF (HKUST-1) irreversibly decomposes to form much larger Cu nanostructures. As shown in the fitting results of *in situ* EXAFS (Fig. 15f–h), Cu–N and Cu–O coordination decreases quickly while Cu–Cu coordination gradually increases with the decrease of the potential. As the applied potential is switched back to 0.64 V *vs.* RHE, the Cu–N coordination dominates the spectrum again, indicating the regeneration of CuPc. The coordination number of Cu–Cu increases obviously after −0.76 V *vs.* RHE and reaches a value of 6.5 around −1.1 V *vs.* RHE, corresponding to the highest CH_4 FE of 66%, suggesting a suitable coordination number for CO_2 methanation.

4.2 *In situ* Raman spectroscopy

In situ Raman spectroscopy is an effective technique for studying the catalyst structure and reaction intermediates during the

CO_2RR.[141–143] Raman spectroscopy involves the analysis of the inelastic scattering of light, providing information about the vibrational modes and molecular structure of the species present in a system. *In situ* Raman spectroscopy allows for real-time monitoring of the reaction intermediates and products, but is not commonly used in CO_2 reduction because of the particularly low intermediate concentration. The signal of intermediates can be clearly detected unless metals with surface enhancement effects, such as Au, Ag, and Cu, are introduced.[144] Additionally, *In situ* Raman spectroscopy enables the investigation of catalyst dynamics and structural changes during CO_2 reduction. It can reveal alterations in the catalyst surface, such as changes in surface roughness, restructuring of active sites, or the formation of reaction byproducts that may affect the catalyst performance. For SSCs, we can track the valence reduction of the metal center during the CO_2RR, which has a great effect on the adsorption of CO_2. Using *in situ*/operando Raman spectroscopy, Ren *et al.* confirmed that the Co center of CoPc was the active site at high currents and more electrons at the Co^{I} center can increase the CO formation rates (Fig. 16a).[145] Both Co^{II} and Co^{I} oxidation states provide diagnostic Raman signatures near 760 and 1140 cm^{-1} in Raman spectra. It is reported that the low conductivity may cause the aggregation of catalytic sites because of electronic isolation, resulting in the coexistence of active Co^{I} sites and inactive Co^{II} sites.[146] With a low CoPc loading of $1.9 \pm 0.5 \times 10^{-7}$ mol cm^{-2} on the GDE, during the CO_2RR, a ratio of $\sim 1:1.35$ for Co^{I} and Co^{II} sites was determined and the primary gaseous product was CO with a low partial current density and high turnover frequency (Fig. 16b). At a high CoPc loading of $9.2 \pm 0.5 \times 10^{-7}$ mol cm^{-2}, CoPc shows more aggregated micrometer-sized particles on the GDE and Co^{II} becomes the dominant species during the CO_2RR (Fig. 16c). The low CO partial current density and low turnover frequency indicate that the increased CoPc was aggregated and does not contribute to CO_2 conversion. By introducing porous carbon nanoparticles (CNPs) with a low CoPc loading of $1.9 \pm 0.5 \times 10^{-7}$ mol cm^{-2} onto the GDE to reduce the aggregation of CoPc, a high CO partial current density and high turnover frequency can be achieved. Operando Raman spectroscopy revealed the percentage of 91.5% for Co^{I} during the CO_2RR (Fig. 16d). These results suggest that dispersing molecular catalysts on a conductive matrix is necessary to ensure the exposure of active sites.

4.3 *In situ* UV-visible spectroscopy

In situ UV-visible spectroscopy is a powerful technique used to investigate the electronic properties and structural changes of catalysts under various conditions. It can be used to study the kinetics and dynamics of reactions, monitor changes in the catalyst's oxidation state, and investigate the stability and degradation of catalyst materials over time. *In situ* UV-visible spectroscopy is well suited for SSCs, especially molecular catalysts like metal phthalocyanine, because the molecular groups have strong adsorption capacity. The working electrode is obtained by depositing catalysts on a transparent platinum sputtered quartz plate, and all the electrodes and gas tubes are inserted into a standard quartz cell (Fig. 17a).[123] As discussed in the results of *in situ* XAS, CuPc would convert into metallic Cu clusters under CO_2RR conditions and convert back to CuPc upon release of the reduction potential. Using *in situ* UV-visible spectroscopy, the decomposition and recovery of CuPc was also confirmed. As shown in Fig. 17b, the reduction of CuPc and the rising absorption of Pc can be observed, corresponding to the formation of Cu^{+} and Cu^{0}. When the working potential returned to OCP, the adsorption of CuPc showed up again. For a carbon dot-supported Cu–N_2O_2 single site catalyst (Cu-CDs), decreasing the electrode potential did not show variation during the CO_2RR (Fig. 17c), indicating the intrinsic activity of the Cu center and the stability of the Cu–N_2O_2 coordination structure.

The options for *in situ* characterization of single-site catalysts for structure tracking are limited. *In situ* XAS is considered one of the most effective techniques which provides valuable information about the electronic and geometric structure of the SSCs during catalytic reactions. However, it is true that the availability of synchrotron light sources, which are necessary for performing *in situ* XAS experiments, limits the laboratory-scale testing of SSCs. Nonetheless, efforts are being made to develop alternative laboratory-based X-ray sources, such as benchtop X-ray absorption spectroscopy instruments, which could potentially broaden the accessibility of *in situ* XAS experiments for SSCs. Additionally, the development of alternative *in situ* characterization techniques for tracking the structural changes of SSCs is of great importance. Diversifying the range of available methods can provide complementary insights into the dynamic behavior of SSCs during catalytic reactions. By exploring and advancing other *in situ* characterization techniques, researchers can broaden their understanding of SSCs and their structural transformations, paving the way for improved catalyst design and performance optimization.

5. Conclusions and perspectives

This review presents the first comprehensive discussion of the reaction mechanism, activity descriptors, and catalyst design for electrochemical CO_2 methanation over single-site catalysts. Firstly, the factors affecting the catalytic activity of CO_2 methanation are discussed, mainly the ligand environment, including the catalyst ligand structure and the reaction environment. In conjunction with the ligand structure design, we detail three main types of single-site catalysts for CO_2 methanation. Most Cu-based catalysts are obviously more competent in adsorbing intermediate products and achieving multi-electron transfer. Appropriate ligand structure design can effectively inhibit the formation of multi-carbon products on copper-based SSCs, thus improving the selectivity of methane. So far, CO_2 methanation over SSCs has achieved high selectivity. Still, its current density, turnover frequency, and stability performance have not yet met the requirements of large-scale operation for industrialization. The option of *in situ* characterization studies also limits the investigation of the dynamic changes of active sites. In this regard, the following several potential perspectives could be helpful for SSCs to achieve industrial CO_2 methanation.

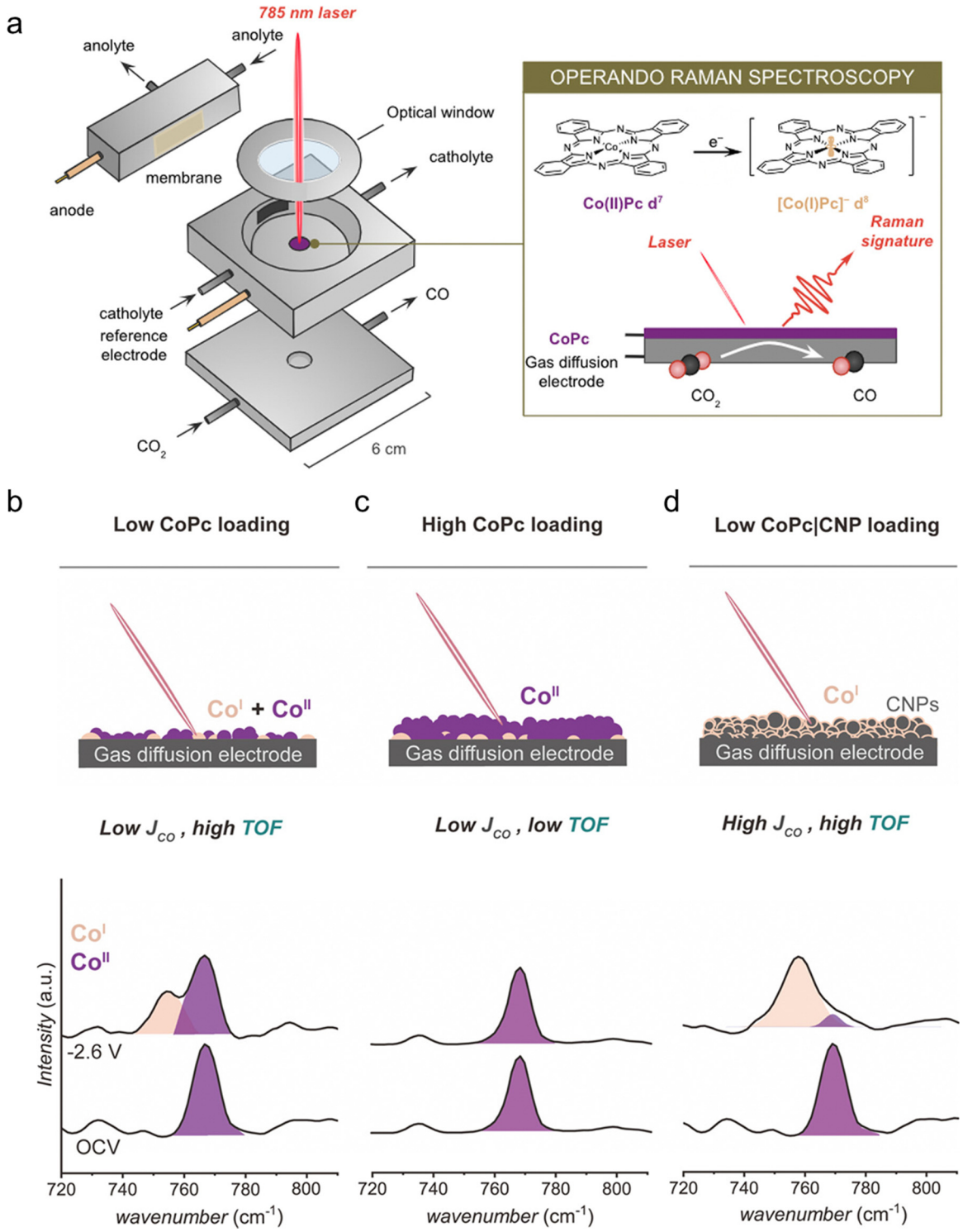

Fig. 16 (a) Operando Raman spectroscopy electrochemical flow cell for the operando detection of active site variation in immobilized molecular electrocatalysts. The distribution of Co^{I} and Co^{II} sites in CoPc molecular catalysts determined by operando Raman spectroscopy for (b) low CoPc loading, (c) high CoPc loading, and (d) low CoPc/CNP loading. Reproduced with permission from Berlinguette *et al.*[145] Copyright 2023 American Chemical Society.

(1) Developing non-Cu-based SSCs

Cu-Based catalysts reduce CO_2 well but have poor single-product selectivity. On the other hand, other metal catalysts are more selective for C_1 products, although obtaining methane from CO_2 is challenging. Although single-site copper catalysts can inhibit the formation of C_2 products, the catalyst reconfiguration during the reaction may still lead to the emergence of Cu particulate species, resulting in increased C_2 product selectivity.

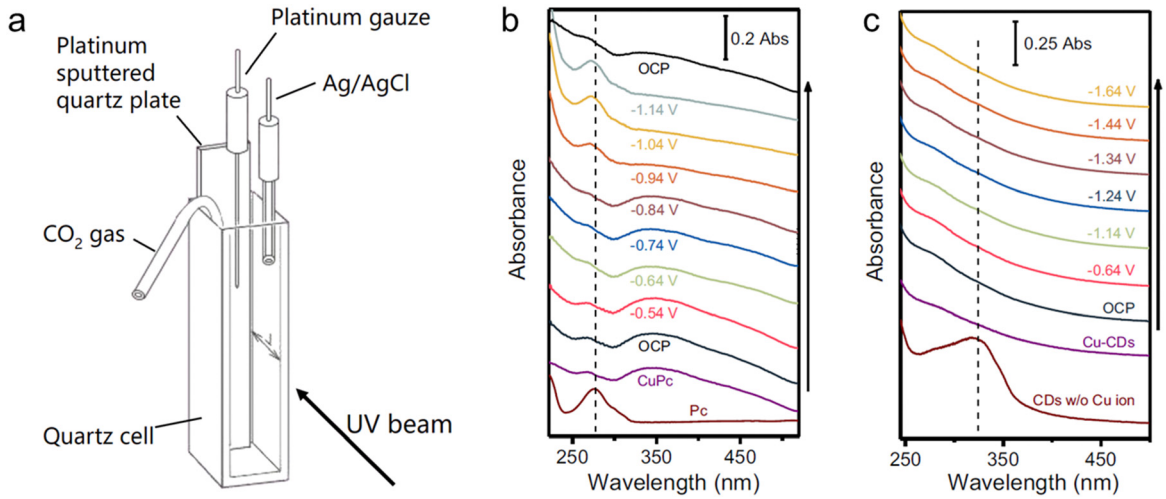

Fig. 17 (a) Schematic illustration of the *in situ* UV-visible spectroscopy setup. *In situ* UV-visible spectra of (b) CuPc and (c) Cu-CDs. Reproduced with permission from Zhu *et al.*[123] Copyright 2021 Springer Nature.

Therefore, a more feasible route is optimizing non-Cu-based single-site catalysts for near 100% selective methane production.

(2) Developing a characterization technology with a higher spatial and temporal resolution

SSCs exhibit different structural stability with different coordination structures. The single metal sites coordinated with O/N are incredibly stable, while the metal–N_4 structure quickly transforms into metal monomers under bias. Similarly, the CO_2RR performance of nanoparticles varies considerably as compared to SSCs. Therefore, more *in situ* characterization methods should be developed to establish the relationship between the coordination structure and performance than just *in situ* XAS and *in situ* Raman.

(3) Preparing high mass-loading SSCs

SSCs with high mass loadings are required for industrial applications, yet developing SSCs with a mass loading of more than 5% remains a significant challenge. Therefore, coordination and morphology structure should be appropriately designed to ensure a high mass loading and the full exposure of active sites.

(4) CO_2 methanation in acidic electrolytes

Although CO_2 methanation is more likely to occur in a proton-rich environment, practically all studies in the present literature are based on neutral and simple media. The fact that the HER is extremely active in acidic electrolytes is another significant challenge. Besides, suppose CO_2 occupies a single active site in SSCs. In that case, the protons cannot be adsorbed on active sites, which limits the HER and efficient CO_2 methanation can be achieved in acidic electrolytes. Therefore, it is vital to regulate the coordination environment of single active sites to enhance the capacity of active sites for CO_2 adsorption than the proton.

(5) Developing a CO_2–CO–CH_4 tandem system

CO is an important intermediate for CO_2 methanation. The CO selectivity close to 100% is achieved for many kinds of SSCs. Thus, developing a system that involves the conversion of CO_2 into CO and then further into methane CH_4 on different cell systems may help stabilize the *CO intermediate and promote the protonation process.

(6) The industrial application of electrochemical CO_2 methanation

Although CO_2 methanation holds promise as an environmentally friendly solution for converting CO_2 emissions into a useful energy source, thus contributing to a reduction in greenhouse gas emissions. However, on an industrial scale, the resulting methane gas must be stored in a controlled manner to prevent its leakage from making the greenhouse effect worse. At the same time, the utilization rate of CO_2 also deeply affects whether the process is environmentally friendly. Ensuring the durability of the electrochemical cells and systems used in this process is vital for minimizing maintenance costs and maximizing the lifespan of the equipment. In addition to these, widespread adoption of this technology in various industries may require incentivizing policies and public awareness campaigns to encourage its use.

Conflicts of interest

The authors declare no conflicts of interest.

Acknowledgements

L. M. acknowledges the National Key Research and Development Program of China (2020YFA0715000), the National Natural Science Foundation of China (51832004, 52127816), and the National Energy-Saving and Low-Carbon Materials Production and Application Demonstration Platform Program (TC220H06N). S. C. acknowledges the "Young Talent Support Plan" of Xi'an Jiaotong University (71211223010707).

References

1 P. De Luna, C. Hahn, D. Higgins, S. A. Jaffer, T. F. Jaramillo and E. H. Sargent, *Science*, 2019, **364**, eaav3506.
2 O. S. Bushuyev, P. De Luna, C. T. Dinh, L. Tao, G. Saur, J. van de Lagemaat, S. O. Kelley and E. H. Sargent, *Joule*, 2018, **2**, 825–832.
3 A. Ozden, F. P. García de Arquer, J. E. Huang, J. Wicks, J. Sisler, R. K. Miao, C. P. O'Brien, G. Lee, X. Wang and A. H. Ip, *Nat. Sustain.*, 2022, **5**, 563–573.
4 M. G. Kibria, J. P. Edwards, C. M. Gabardo, C. T. Dinh, A. Seifitokaldani, D. Sinton and E. H. Sargent, *Adv. Mater.*, 2019, **31**, 1807166.
5 O. Hoegh-Guldberg, D. Jacob, M. Taylor, T. Guillén Bolaños, M. Bindi, S. Brown, I. A. Camilloni, A. Diedhiou, R. Djalante and K. Ebi, *Science*, 2019, **365**, eaaw6974.
6 Y. Quan, J. Zhu and G. Zheng, *Small Sci.*, 2021, **1**, 2100043.
7 J. E. Huang, F. Li, A. Ozden, A. Sedighian Rasouli, F. P. García de Arquer, S. Liu, S. Zhang, M. Luo, X. Wang and Y. Lum, *Science*, 2021, **372**, 1074–1078.
8 Y. Li, A. Ozden, W. R. Leow, P. Ou, J. E. Huang, Y. Wang, K. Bertens, Y. Xu, Y. Liu and C. Roy, *Nat. Catal.*, 2022, **5**, 185–192.
9 J. Wicks, M. L. Jue, V. A. Beck, J. S. Oakdale, N. A. Dudukovic, A. L. Clemens, S. Liang, M. E. Ellis, G. Lee and S. E. Baker, *Adv. Mater.*, 2021, **33**, 2003855.
10 Z. Zhang, E. W. Lees, F. Habibzadeh, D. A. Salvatore, S. Ren, G. L. Simpson, D. G. Wheeler, A. Liu and C. P. Berlinguette, *Energy Environ. Sci.*, 2022, **15**, 705–713.
11 S. Nitopi, E. Bertheussen, S. B. Scott, X. Liu, A. K. Engstfeld, S. Horch, B. Seger, I. E. L. Stephens, K. Chan and C. Hahn, *Chem. Rev.*, 2019, **119**, 7610–7672.
12 S. Navarro-Jaén, M. Virginie, J. Bonin, M. Robert, R. Wojcieszak and A. Y. Khodakov, *Nat. Rev. Chem.*, 2021, **5**, 564–579.
13 Y. Wang, Y. Zheng, C. Han and W. Chen, *Nano Res.*, 2021, **14**, 1682–1697.
14 P. Zhu, X. Xiong and D. Wang, *Nano Res.*, 2022, **15**, 5792–5815.
15 H. Jing, P. Zhu, X. Zheng, Z. Zhang, D. Wang and Y. Li, *Adv. Powder Mater.*, 2022, **1**, 100013.
16 J. Zhu, J. Li, R. Lu, R. Yu, S. Zhao, C. Li, L. Lv, L. Xia, X. Chen and W. Cai, *Nat. Commun.*, 2023, **14**, 4670.
17 W. Zong, H. Gao, Y. Ouyang, K. Chu, H. Guo, L. Zhang, W. Zhang, R. Chen, Y. Dai and F. Guo, *Angew. Chem., Int. Ed.*, 2023, **135**, e202218122.
18 Y. Y. Birdja, E. Pérez-Gallent, M. C. Figueiredo, A. J. Göttle, F. Calle-Vallejo and M. Koper, *Nat. Energy*, 2019, **4**, 732–745.
19 S. Verma, S. Lu and P. J. A. Kenis, *Nat. Energy*, 2019, **4**, 466–474.
20 S. Zhang, Q. Fan, R. Xia and T. J. Meyer, *Acc. Chem. Res.*, 2020, **53**, 255–264.
21 Z. Zhang, J. Zhu, S. Chen, W. Sun and D. Wang, *Angew. Chem., Int. Ed.*, 2022, **62**, e202215136.
22 A. Caballero and P. J. Perez, *Chem. Soc. Rev.*, 2013, **42**, 8809–8820.
23 L. Sun, Y. Wang, N. Guan and L. Li, *Energy Technol.*, 2020, **8**, 1900826.
24 M. Younas, L. Loong Kong, M. J. K. Bashir, H. Nadeem, A. Shehzad and S. Sethupathi, *Energy Fuels*, 2016, **30**, 8815–8831.
25 S. Kattel, P. Liu and J. G. Chen, *J. Am. Chem. Soc.*, 2017, **139**, 9739–9754.
26 C. Vogt, E. Groeneveld, G. Kamsma, M. Nachtegaal, L. Lu, C. J. Kiely, P. H. Berben, F. Meirer and B. M. Weckhuysen, *Nat. Catal.*, 2018, **1**, 127–134.
27 R.-P. Ye, J. Ding, W. Gong, M. D. Argyle, Q. Zhong, Y. Wang, C. K. Russell, Z. Xu, A. G. Russell and Q. Li, *Nat. Commun.*, 2019, **10**, 5698.
28 R. Kortlever, J. Shen, K. J. P. Schouten, F. Calle-Vallejo and M. T. M. Koper, *J. Phys. Chem. L*, 2015, **6**, 4073–4082.
29 K. J. P. Schouten, Z. Qin, E. Pérez Gallent and M. T. M. Koper, *J. Am. Chem. Soc.*, 2012, **134**, 9864–9867.
30 K. J. P. Schouten, Y. Kwon, C. J. M. Van Der Ham, Z. Qin and M. T. M. Koper, *Chem. Sci.*, 2011, **2**, 1902–1909.
31 R. Zhao, P. Ding, P. Wei, L. Zhang, Q. Liu, Y. Luo, T. Li, S. Lu, X. Shi and S. Gao, *Adv. Funct. Mater.*, 2021, **31**, 2009449.
32 Y. Xu, F. Li, A. Xu, J. P. Edwards, S.-F. Hung, C. M. Gabardo, C. P. O'Brien, S. Liu, X. Wang and Y. Li, *Nat. Commun.*, 2021, **12**, 1–7.
33 J. Shen, R. Kortlever, R. Kas, Y. Y. Birdja, O. Diaz-Morales, Y. Kwon, I. Ledezma-Yanez, K. J. P. Schouten, G. Mul and M. Koper, *Nat. Commun.*, 2015, **6**, 1–8.
34 L. Zhang, X.-X. Li, Z.-L. Lang, Y. Liu, J. Liu, L. Yuan, W.-Y. Lu, Y.-S. Xia, L.-Z. Dong and D.-Q. Yuan, *J. Am. Chem. Soc.*, 2021, **143**, 3808–3816.
35 Y. R. Wang, M. Liu, G. K. Gao, Y. L. Yang, R. X. Yang, H. M. Ding, Y. Chen, S. L. Li and Y. Q. Lan, *Angew. Chem., Int. Ed.*, 2021, **60**, 21952–21958.
36 Y. Zhang, L.-Z. Dong, S. Li, X. Huang, J.-N. Chang, J.-H. Wang, J. Zhou, S.-L. Li and Y.-Q. Lan, *Nat. Commun.*, 2021, **12**, 1–9.
37 Y. R. Wang, H. M. Ding, X. Y. Ma, M. Liu, Y. L. Yang, Y. Chen, S. L. Li and Y. Q. Lan, *Angew. Chem., Int. Ed.*, 2022, **61**, e202114648.
38 S. Chen, W. H. Li, W. Jiang, J. Yang, J. Zhu, L. Wang, H. Ou, Z. Zhuang, M. Chen and X. Sun, *Angew. Chem., Int. Ed.*, 2022, **61**, e202114450.
39 G. Shi, Y. Xie, L. Du, X. Fu, X. Chen, W. Xie, T. B. Lu, M. Yuan and M. Wang, *Angew. Chem., Int. Ed.*, 2022, **61**, e202203569.
40 L. Xiong, X. Zhang, L. Chen, Z. Deng, S. Han, Y. Chen, J. Zhong, H. Sun, Y. Lian and B. Yang, *Adv. Mater.*, 2021, **33**, 2101741.
41 Y.-L. Qiu, H.-X. Zhong, T.-T. Zhang, W.-B. Xu, X.-F. Li and H.-M. Zhang, *ACS Catal.*, 2017, **7**, 6302–6310.
42 J. D. Yi, R. Xie, Z. L. Xie, G. L. Chai, T. F. Liu, R. P. Chen, Y. B. Huang and R. Cao, *Angew. Chem., Int. Ed.*, 2020, **59**, 23641–23648.
43 F. P. García de Arquer, C.-T. Dinh, A. Ozden, J. Wicks, C. McCallum, A. R. Kirmani, D.-H. Nam, C. Gabardo, A. Seifitokaldani and X. Wang, *Science*, 2020, **367**, 661–666.
44 G. Wang, J. Chen, Y. Ding, P. Cai, L. Yi, Y. Li, C. Tu, Y. Hou, Z. Wen and L. Dai, *Chem. Soc. Rev.*, 2021, **50**, 4993–5061.
45 J.-C. Jiang, J.-C. Chen, M.-D. Zhao, Q. Yu, Y.-G. Wang and J. Li, *Nano Res.*, 2022, **15**, 7116–7123.

46 S. Chen, B. Wang, J. Zhu, L. Wang, H. Ou, Z. Zhang, X. Liang, L. Zheng, L. Zhou and Y.-Q. Su, *Nano Lett.*, 2021, **21**, 7325–7331.
47 Y. Cai, J. Fu, Y. Zhou, Y.-C. Chang, Q. Min, J.-J. Zhu, Y. Lin and W. Zhu, *Nat. Commun.*, 2021, **12**, 1–9.
48 H.-L. Zhu, J.-R. Huang, X.-W. Zhang, C. Wang, N.-Y. Huang, P.-Q. Liao and X.-M. Chen, *ACS Catal.*, 2021, **11**, 11786–11792.
49 Z. Han, D. Han, Z. Chen, J. Gao, G. Jiang, X. Wang, S. Lyu, Y. Guo, C. Geng and L. Yin, *Nat. Commun.*, 2022, **13**, 1–10.
50 X. Zheng, B. Li, Q. Wang, D. Wang and Y. Li, *Nano Res.*, 2022, **15**, 7806–7839.
51 R. Ding, M. Ma, Y. Chen, X. Wang, J. Li, G. Wang and J. Liu, *Nano Res.*, 2023, **16**, 264–280.
52 G. Huang, Q. Niu, Y. He, J. Tian, M. Gao, C. Li, N. An, J. Bi and J. Zhang, *Nano Res.*, 2022, **15**, 8001–8009.
53 G. Wang, Y. Wu, Z. Li, Z. Lou, Q. Chen, Y. Li, D. Wang and J. Mao, *Angew. Chem., Int. Ed.*, 2023, **62**, e202218460.
54 T. Gan and D. Wang, *Nano Res.*, 2023, 1–21.
55 Z. Wang, Q. Yuan, J. Shan, Z. Jiang, P. Xu, Y. Hu, J. Zhou, L. Wu, Z. Niu and J. Sun, *J. Phys. Chem. L*, 2020, **11**, 7261–7266.
56 H. Hashiba, H. K. Sato, S. Yotsuhashi, K. Fujii, M. Sugiyama and Y. Nakano, *Sustainable Energy Fuels*, 2017, **1**, 1734–1739.
57 H. Pan and C. J. Barile, *Energy Environ. Sci.*, 2020, **13**, 3567–3578.
58 Y. Hori, A. Murata and R. Takahashi, *J. Chem. Soc., Faraday Trans. 1*, 1989, **85**, 2309–2326.
59 J. J. Kim, D. P. Summers and K. W. Frese Jr, *J. Electroanal. Chem. Interfacial Electrochem.*, 1988, **245**, 223–244.
60 Z. Sun, T. Ma, H. Tao, Q. Fan and B. Han, *Chem*, 2017, **3**, 560–587.
61 J. Shen and D. Wang, *Nano Res. Energy*, 2023, **2**, e9120096.
62 W. Luo, X. Nie, M. J. Janik and A. Asthagiri, *ACS Catal.*, 2016, **6**, 219–229.
63 C. Xie, Z. Niu, D. Kim, M. Li and P. Yang, *Chem. Rev.*, 2019, **120**, 1184–1249.
64 Y. Hori, H. Wakebe, T. Tsukamoto and O. Koga, *Surf. Sci.*, 1995, **335**, 258–263.
65 Y. Hori, I. Takahashi, O. Koga and N. Hoshi, *J. Mol. Catal. A: Chem.*, 2003, **199**, 39–47.
66 D. Gao, R. M. Arán-Ais, H. S. Jeon and B. Roldan Cuenya, *Nat. Catal.*, 2019, **2**, 198–210.
67 R. Reske, H. Mistry, F. Behafarid, B. Roldan Cuenya and P. Strasser, *J. Am. Chem. Soc.*, 2014, **136**, 6978–6986.
68 Z. Zhuang, L. Xia, J. Huang, P. Zhu, Y. Li, C. Ye, M. Xia, R. Yu, Z. Lang and J. Zhu, *Angew. Chem., Int. Ed.*, 2022, **62**, e202212335.
69 Z. Liu, Y. Du, R. Yu, M. Zheng, R. Hu, J. Wu, Y. Xia, Z. Zhuang and D. Wang, *Angew. Chem., Int. Ed.*, 2022, **62**, e202212653.
70 R. Li and D. Wang, *Nano Res.*, 2022, **15**, 6888–6923.
71 J. Yang, W. H. Li, K. Xu, S. Tan, D. Wang and Y. Li, *Angew. Chem., Int. Ed.*, 2022, **134**, e202200366.
72 E. Zhang, L. Tao, J. An, J. Zhang, L. Meng, X. Zheng, Y. Wang, N. Li, S. Du and J. Zhang, *Angew. Chem., Int. Ed.*, 2022, **134**, e202117347.
73 S. Ning, H. Ou, Y. Li, C. Lv, S. Wang, D. Wang and J. Ye, *Angew. Chem., Int. Ed.*, 2023, **62**, e202302253.
74 L. Wang, H. Liu, J. Zhuang and D. Wang, *Small Sci.*, 2022, **2**, 2200036.
75 Q. Wang, X. Zheng, J. Wu, Y. Wang, D. Wang and Y. Li, *Small Struct.*, 2022, **3**, 2200059.
76 A. M. Argo, J. F. Odzak and B. C. Gates, *J. Am. Chem. Soc.*, 2003, **125**, 7107–7115.
77 C. J. H. Jacobsen, S. Dahl, P. L. Hansen, E. Törnqvist, L. Jensen, H. Topsøe, D. V. Prip, P. B. Møenshaug and I. Chorkendorff, *J. Mol. Catal. A: Chem.*, 2000, **163**, 19–26.
78 W. H. Li, B. C. Ye, J. Yang, Y. Wang, C. J. Yang, Y. M. Pan, H. T. Tang, D. Wang and Y. Li, *Angew. Chem., Int. Ed.*, 2022, **61**, e202209749.
79 K. Manthiram, B. J. Beberwyck and A. P. Alivisatos, *J. Am. Chem. Soc.*, 2014, **136**, 13319–13325.
80 Q. Hu, Z. Han, X. Wang, G. Li, Z. Wang, X. Huang, H. Yang, X. Ren, Q. Zhang and J. Liu, *Angew. Chem., Int. Ed.*, 2020, **59**, 19054–19059.
81 W. H. Li, J. Yang and D. Wang, *Angew. Chem., Int. Ed.*, 2022, **61**, e202213318.
82 T. Cui, Y. P. Wang, T. Ye, J. Wu, Z. Chen, J. Li, Y. Lei, D. Wang and Y. Li, *Angew. Chem., Int. Ed.*, 2022, **61**, e202115219.
83 X. Zheng, J. Yang, Z. Xu, Q. Wang, J. Wu, E. Zhang, S. Dou, W. Sun, D. Wang and Y. Li, *Angew. Chem., Int. Ed.*, 2022, **61**, e202205946.
84 B. Wang, C. Cheng, M. Jin, J. He, H. Zhang, W. Ren, J. Li, D. Wang and Y. Li, *Angew. Chem., Int. Ed.*, 2022, **134**, e202207268.
85 M. Qu, Z. Chen, Z. Sun, D. Zhou, W. Xu, H. Tang, H. Gu, T. Liang, P. Hu and G. Li, *Nano Res.*, 2023, **16**, 2170–2176.
86 F. Yang, H. Yu, Y. Su, J. Chen, S. Chen, Z. Zeng, S. Deng and J. Wang, *Nano Res.*, 2023, **16**, 146–154.
87 A. Han, W. Sun, X. Wan, D. Cai, X. Wang, F. Li, J. Shui and D. Wang, *Angew. Chem., Int. Ed.*, 2023, **62**, e202303185.
88 X. Zheng, J. Yang, P. Li, Z. Jiang, P. Zhu, Q. Wang, J. Wu, E. Zhang, W. Sun and S. Dou, *Angew. Chem., Int. Ed.*, 2023, **62**, e202217449.
89 A. Bagger, W. Ju, A. S. Varela, P. Strasser and J. Rossmeisl, *ACS Catal.*, 2019, **9**, 7894–7899.
90 Y. Xu, F. Li, A. Xu, J. P. Edwards, S.-F. Hung, C. M. Gabardo, C. P. O'Brien, S. Liu, X. Wang and Y. Li, *Nat. Commun.*, 2021, **12**, 2932.
91 Y. Hori, R. Takahashi, Y. Yoshinami and A. Murata, *J. Phys. Chem. B*, 1997, **101**, 7075–7081.
92 N. Gupta, M. Gattrell and B. MacDougall, *J. Appl. Electrochem.*, 2006, **36**, 161–172.
93 C.-T. Dinh, T. Burdyny, M. G. Kibria, A. Seifitokaldani, C. M. Gabardo, F. P. García de Arquer, A. Kiani, J. P. Edwards, P. De Luna and O. S. Bushuyev, *Science*, 2018, **360**, 783–787.
94 H. S. Jeon, J. Timoshenko, C. Rettenmaier, A. Herzog, A. Yoon, S. W. Chee, S. Oener, U. Hejral, F. T. Haase and B. Roldan Cuenya, *J. Am. Chem. Soc.*, 2021, **143**, 7578–7587.
95 J. Zhu, L. Xia, R. Yu, R. Lu, J. Li, R. He, Y. Wu, W. Zhang, X. Hong and W. Chen, *J. Am. Chem. Soc.*, 2022, **144**, 15529–15538.

96 Y. Gao, B. Liu and D. Wang, *Adv. Mater.*, 2023, **35**, 2209654.
97 A. Murata and Y. Hori, *Bull. Chem. Soc. Jpn.*, 1991, **64**, 123–127.
98 G. Z. Kyriacou and A. K. Anagnostopoulos, *J. Appl. Electrochem.*, 1993, **23**, 483–486.
99 A. S. Varela, W. Ju, T. Reier and P. Strasser, *ACS Catal.*, 2016, **6**, 2136–2144.
100 J. Resasco, Y. Lum, E. Clark, J. Z. Zeledon and A. T. Bell, *Chem. Electro. Chem.*, 2018, **5**, 1064–1072.
101 X. Wang, P. Ou, J. Wicks, Y. Xie, Y. Wang, J. Li, J. Tam, D. Ren, J. Y. Howe and Z. Wang, *Nat. Commun.*, 2021, **12**, 3387.
102 H. Zhang, X. Chang, J. G. Chen, W. A. Goddard Iii, B. Xu, M.-J. Cheng and Q. Lu, *Nat. Commun.*, 2019, **10**, 3340.
103 C. F. C. Lim, D. A. Harrington and A. T. Marshall, *Electrochim. Acta*, 2017, **238**, 56–63.
104 H. Zhang, X. Chang, J. G. Chen, W. A. Goddard, B. Xu, M.-J. Cheng and Q. Lu, *Nat. Commun.*, 2019, **10**, 1–9.
105 X. Wang, P. Ou, J. Wicks, Y. Xie, Y. Wang, J. Li, J. Tam, D. Ren, J. Y. Howe and Z. Wang, *Nat. Commun.*, 2021, **12**, 1–7.
106 C. G. Morales-Guio, E. R. Cave, S. A. Nitopi, J. T. Feaster, L. Wang, K. P. Kuhl, A. Jackson, N. C. Johnson, D. N. Abram and T. Hatsukade, *Nat. Catal.*, 2018, **1**, 764–771.
107 S. Wei, X. Jiang, C. He, S. Wang, Q. Hu, X. Chai, X. Ren, H. Yang and C. He, *J. Mater. Chem. A*, 2022, **10**, 6187–6192.
108 Q. Zhao, Y. Wang, M. Li, S. Zhu, T. Li, J. Yang, T. Lin, E. P. Delmo, Y. Wang and J. Jang, *SmartMat*, 2022, **3**, 183–193.
109 L. Lin, T. Liu, J. Xiao, H. Li, P. Wei, D. Gao, B. Nan, R. Si, G. Wang and X. Bao, *Angew. Chem., Int. Ed.*, 2020, **59**, 22408–22413.
110 H. Zou, G. Zhao, H. Dai, H. Dong, W. Luo, L. Wang, Z. Lu, Y. Luo, G. Zhang and L. Duan, *Angew. Chem., Int. Ed.*, 2022, **62**, e202217220.
111 Y. Wang, Z. Chen, P. Han, Y. Du, Z. Gu, X. Xu and G. Zheng, *ACS Catal.*, 2018, **8**, 7113–7119.
112 L. Xue, C. Zhang, J. Wu, Q.-Y. Fan, Y. Liu, Y. Wu, J. Li, H. Zhang, F. Liu and S. Zeng, *Appl. Catal., B*, 2022, **304**, 120951.
113 S. Chen, Z. Zhang, W. Jiang, S. Zhang, J. Zhu, L. Wang, H. Ou, S. Zaman, L. Tan and P. Zhu, *J. Am. Chem. Soc.*, 2022, **144**, 12807–12815.
114 B. J. Fisher and R. Eisenberg, *J. Am. Chem. Soc.*, 1980, **102**, 7361–7363.
115 N. Furuya and K. Matsui, *J. Electroanal. Chem. Interfacial Electrochem.*, 1989, **271**, 181–191.
116 J. Shen, R. Kortlever, R. Kas, Y. Y. Birdja, O. Diaz-Morales, Y. Kwon, I. Ledezma-Yanez, K. J. P. Schouten, G. Mul and M. T. M. Koper, *Nat. Commun.*, 2015, **6**, 8177.
117 H. Xiao, W. A. Goddard Iii, T. Cheng and Y. Liu, *Proc. Natl. Acad. Sci. U. S. A.*, 2017, **114**, 6685–6688.
118 L. L. Zhuo, P. Chen, K. Zheng, X. W. Zhang, J. X. Wu, D. Y. Lin, S. Y. Liu, Z. S. Wang, J. Y. Liu and D. D. Zhou, *Angew. Chem., Int. Ed.*, 2022, **134**, e202204967.
119 A. Guan, Z. Chen, Y. Quan, C. Peng, Z. Wang, T.-K. Sham, C. Yang, Y. Ji, L. Qian and X. Xu, *ACS Energy Lett.*, 2020, **5**, 1044–1053.
120 W. Ju, A. Bagger, X. Wang, Y. Tsai, F. Luo, T. Möller, H. Wang, J. Rossmeisl, A. S. Varela and P. Strasser, *ACS Energy Lett.*, 2019, **4**, 1663–1671.
121 J. Wang, M. Zheng, X. Zhao and W. Fan, *ACS Catal.*, 2022, **12**, 5441–5454.
122 S. Ren, D. Joulié, D. Salvatore, K. Torbensen, M. Wang, M. Robert and C. P. Berlinguette, *Science*, 2019, **365**, 367–369.
123 Y. Cai, J. Fu, Y. Zhou, Y.-C. Chang, Q. Min, J.-J. Zhu, Y. Lin and W. Zhu, *Nat. Commun.*, 2021, **12**, 586.
124 C. Huang, Y. Li, N. Wang, Y. Xue, Z. Zuo, H. Liu and Y. Li, *Chem. Rev.*, 2018, **118**, 7744–7803.
125 X. Gao, H. Liu, D. Wang and J. Zhang, *Chem. Soc. Rev.*, 2019, **48**, 908–936.
126 R. Lang, X. Du, Y. Huang, X. Jiang, Q. Zhang, Y. Guo, K. Liu, B. Qiao, A. Wang and T. Zhang, *Chem. Rev.*, 2020, **120**, 11986–12043.
127 K. L. Zhou, Z. Wang, C. B. Han, X. Ke, C. Wang, Y. Jin, Q. Zhang, J. Liu, H. Wang and H. Yan, *Nat. Commun.*, 2021, **12**, 1–10.
128 D. Gao, Y. Zhang, Z. Zhou, F. Cai, X. Zhao, W. Huang, Y. Li, J. Zhu, P. Liu and F. Yang, *J. Am. Chem. Soc.*, 2017, **139**, 5652–5655.
129 L. Lv, R. Lu, J. Zhu, R. Yu, W. Zhang, E. Cui, X. Chen, Y. Dai, L. Cui and J. Li, *Angew. Chem., Int. Ed.*, 2023, **62**, e202303117.
130 Z. Zhang, S. Chen, J. Zhu, C. Ye, Y. Mao, B. Wang, G. Zhou, L. Mai, Z. Wang and X. Liu, *Nano Lett.*, 2023, **23**, 2312–2320.
131 Y. Jiang, Q. Chen, D. Wang, X. Li, Y. Xu, Z. Xu and G. Guo, *Nano Res.*, 2023, **16**, 6661–6669.
132 J. Xu, S. Yang, L. Ji, J. Mao, W. Zhang, X. Zheng, H. Fu, M. Yuan, C. Yang and H. Chen, *Nano Res.*, 2023, **16**, 53–61.
133 Z. Weng, Y. Wu, M. Wang, J. Jiang, K. Yang, S. Huo, X.-F. Wang, Q. Ma, G. W. Brudvig and V. S. Batista, *Nat. Commun.*, 2018, **9**, 415.
134 A. D. Handoko, F. Wei, Jenndy, B. S. Yeo and Z. W. Seh, *Nat. Catal.*, 2018, **1**, 922–934.
135 S.-F. Hung, A. Xu, X. Wang, F. Li, S.-H. Hsu, Y. Li, J. Wicks, E. G. Cervantes, A. S. Rasouli and Y. C. Li, *Nat. Commun.*, 2022, **13**, 819.
136 D. Karapinar, N. T. Huan, N. Ranjbar Sahraie, J. Li, D. Wakerley, N. Touati, S. Zanna, D. Taverna, L. H. Galvão Tizei and A. Zitolo, *Angew. Chem., Int. Ed.*, 2019, **58**, 15098–15103.
137 Z. Zhang, J. Zhu, S. Chen, W. Sun and D. Wang, *Angew. Chem., Int. Ed.*, 2023, **135**, e202215136.
138 X. Li, X. Yang, J. Zhang, Y. Huang and B. Liu, *ACS Catal.*, 2019, **9**, 2521–2531.
139 D. Zang, X. J. Gao, L. Li, Y. Wei and H. Wang, *Nano Res.*, 2022, **15**, 8872–8879.
140 C. E. Creissen and M. Fontecave, *Nat. Commun.*, 2022, **13**, 2280.
141 J. Zhang, X. Song, L. Kang, J. Zhu, L. Liu, Q. Zhang, D. J. L. Brett, P. R. Shearing, L. Mai and I. P. Parkin, *Chem. Catal.*, 2022, **2**, 3254–3270.
142 W. Wang, X. Wang, Z. Ma, Y. Wang, Z. Yang, J. Zhu, L. Lv, H. Ning, N. Tsubaki and M. Wu, *ACS Catal.*, 2022, **13**, 796–802.

143 W. Zhang, C. Huang, J. Zhu, Q. Zhou, R. Yu, Y. Wang, P. An, J. Zhang, M. Qiu and L. Zhou, *Angew. Chem., Int. Ed.*, 2022, **61**, e202112116.
144 X. Li, S. Wang, L. Li, Y. Sun and Y. Xie, *J. Am. Chem. Soc.*, 2020, **142**, 9567–9581.
145 S. Ren, E. W. Lees, C. Hunt, A. Jewlal, Y. Kim, Z. Zhang, B. A. W. Mowbray, A. G. Fink, L. Melo and E. R. Grant, *J. Am. Chem. Soc.*, 2023, **145**, 4414–4420.
146 N. Corbin, J. Zeng, K. Williams and K. Manthiram, *Nano Res.*, 2019, **12**, 2093–2125.